2019

MECHANICAL RESPONSE OF POLYMER-FABRIC SKIN MATERIALS USED IN INFLATABLE DROP-STITCH STRUCTURES

Michael P. Smith
University of Rhode Island, michael_smith95@my.uri.edu

MECHANICAL RESPONSE OF POLYMER-FABRIC SKIN MATERIALS USED IN INFLATABLE DROP-STITCH STRUCTURES

BY

MICHAEL P. SMITH

A THESIS SUBMITTED IN PARTIAL FULFILLMENT OF THE

REQUIREMENTS FOR THE DEGREE OF

MASTER OF SCIENCE

IN

MECHANICAL ENGINEERING

UNIVERSITY OF RHODE ISLAND

2019

MASTER OF SCIENCE THESIS

OF

MICHAEL P. SMITH

APPROVED:

Thesis Committee:

Major Professor David G. Taggart

Hongyan Yuan

George Tsiatas

Nasser H. Zawia

DEAN OF THE GRADUATE SCHOOL

UNIVERSITY OF RHODE ISLAND

2019

ABSTRACT

The rapid deployment capabilities of drop-stitch inflatable structures is of increasing significance for aerospace, naval, and military applications. The drop-stitch inflatable structures have a high load capacity, low manufacturing cost, low weight, and low storage volume. These properties make such inflatable structures ideal for applications where the rapid deployment of structures is crucial, such as in aerospace, naval, and military applications. The rigidity of such structures increases with the inflation pressure of the structure and is dependent on the properties of the composite neoprene-fabric skin material.

The objective of this research is to determine the mechanical response of the composite neoprene-fabric material used in drop-stitch inflatable structures under uniaxial loading such that a more accurate model for the mechanical behavior of inflatable woven fabric drop-stitch composite structures may be developed. This research utilizes digital image correlation (DIC) techniques in order to noninvasively measure the behavior of the skin material under uniaxial loading.

The behavior of an inflatable drop-stitch panel under four-point bending is analyzed and compared to theoretical results using the experimentally calculated properties of the skin material. The deformation due to bending and shear are both calculated and compared to the experimental data. Additionally, an empirical parameter is introduced to the classical beam theory equation for panel deflection under four-point bending in order to account for kinking of the panel at the load points.

The results of this research found the relevant properties of the skin material which are used in the panel modeling. The comparison of the four-point bending model and experimental data demonstrated that the classical beam theory is not sufficient for modeling drop-stitch inflatable structure behavior, especially at low

internal pressure. The shear deformation and deformation mechanics of the drop-stitch inflatable structures were found to be significant to the overall mechanical response of the panels.

ACKNOWLEDGMENTS

I would like to thank my major professor and advisor Dr. David Taggart for his guidance and support throughout this research. I greatly appreciate the technical and professional support he has given me throughout our time working together. I am also grateful for the patience and assistance he has given me over the time we have worked together.

I would also like to thank Milo Ferrazzoli and Alena Alich for their contributions to this research, both in technical assistance and conceptual ideas. Working together with them under Dr. Taggart's guidance has been a great experience, and I appreciate everything that they have done to help me achieve my goals. I would also like to thank Scott Liguori and Trevor Ide for their assistance in running experiments and generating data.

I must also thank the Department of Civil and Environmental Engineering as well as Dr. George Tsiatas for the use of the structures laboratory for this research. I also extend my gratitude to the Department of Mechanical, Industrial, and Systems Engineering and the University of Rhode Island as a whole for the opportunities given to me here.

I would also like to extend my gratitude to the Office of Naval Research (ONR) for the continued funding and support of this research.

Lastly I would like to thank my family for all of the support they have given me throughout the years of my education. Their love and support have really helped me get to where I am today.

Contents

Page

Page

List of Figures

Figure **Page**

List of Tables

CHAPTER 1

Introduction

Inflatable fabric structures are of increasing importance in military and aerospace applications due to the minimal weight, small packaging volume, rapid deployment capabilities, and low transportation costs. Inflatable structures are a type of structure that derives its rigidity and structural integrity from the use of internal pressurized air inflating a pliable material envelope (Sadegh and Cavallaro, 2006). The inflatable fabric structures investigated in this research are drop-stitch inflatable structures currently developed for naval and space applications.

1.1 Overview of Drop-Stitch Inflatable Structures

Drop-stitch inflatable structures are characterized by stitches connecting the flat faces of the panel. The addition of drop-stitches allows for the panel to maintain constant depth across the major face of the panel.

Example applications of drop-stitch inflatable structures include rapid deployment shelters, hangars, inflatable temporary storage units, and mobile decontamination chambers (Barnfield, 2016). Drop-stitch inflatable panels are also of use in watercraft such as kayaks (Halswell et al., 2012) and in spacecraft (Comer and Levy, 1963). An example of the application of drop-stitch panels in an inflatable kayak is provided in Figure 1. Notice that the walls of the kayak are composed of individual drop-stitch panels. These inflatable kayaks and similar inflatable watercraft are useful due to the small storage volume and rapid deployment capabilities.

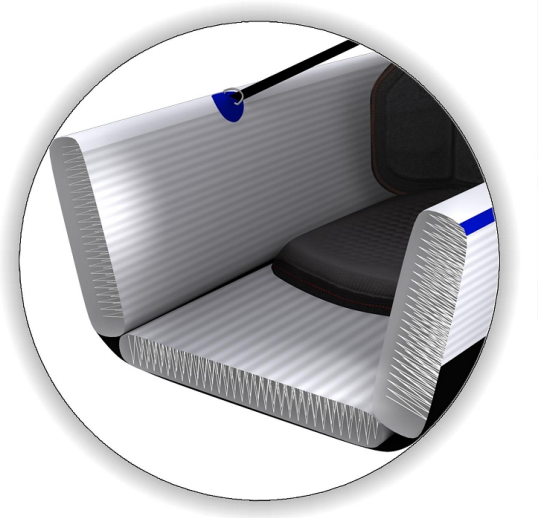

Figure 1. Example of Drop-Stitch Panel Configuration in Inflatable Kayaks (Hodge, 2018)

An example of a hangar utilizing drop-stitch panels is also provided in Figure 2. The benefit for inflatable shelters such as the hangar shown are also the rapid deployment capabilities, small storage volume, and ease of deconstruction.

Figure 2. Example of Aircraft Hangar Utilizing Drop-Stitch Panels (Barnfield, 2016)

The general configuration of the drop-stitch inflatable structure layers is shown in Figure 3. Note that the laminated skin is normally a fabric chafer layer embedded in a polymer coating, primarily neoprene. The drop stitching is tied into the connecting woven fabric layer.

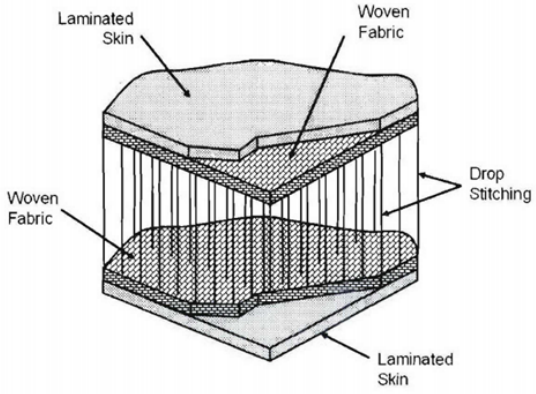

Figure 3. General Configuration of Drop-Stitch Inflatable Fabric Structures (Sadegh and Cavallaro, 2006)

The inflation of the drop-stitch inflatable structure applies internal pretension to the envelope and drop-stitches. The pretension of the skin and drop-stitches provides rigidity to the structure, however the nature of the rigidity is dependent on the mechanical properties of the composite fabric skin in the axial and transverse directions (Felicissimo, 2015). The drop-stitches are anchored to the panel skin material under biaxial loading. The complex loading of this skin material further complicates the precise modeling of these drop-stitch woven inflatable panels.

1.2 Motivation

The challenge in accurately modeling inflatable drop-stitch fabric structures has been in the modeling of the complex loading of the panels due to the pressurized air (Graczykowski and Heinonen, 2006). The modeling of the panel skin properties also proves challenging due to the nonlinear behavior of the woven fabric skin material (Sadegh and Cavallaro, 2012).

The simplest approximation commonly used for design using inflatable drop-stitch fabric structures is to treat the beams as an Euler-Bernoulli beam. Euler-Bernoulli or "classical" beam theory assumes that the cross-sections of the beam remain planar and normal to the midplane (Ho, 2015). The method that is commonly

used assumes that the properties of the skin may be approximated as pressure dependent. Pressure dependent skin properties are typically determined through correlation with inflated panel bending data.

The approach of approximating panels as Euler-Bernoulli beams has been used since the initial research into inflatable structures for use in spacecraft and orbital deployment in the early 1960s (Comer and Levy, 1963). Theoretical and experimental investigations into the applications and functionality of inflatable structures since then, however, have argued that the simple approximation does not adequately account for the deformation mechanism within inflatable structures (Van and Wielgosz, 2005).

An investigation to verify that the difference between the approximation using the Euler-Bernoulli model and the experimental performance of the beam are significant, is therefore performed and compared with relevant literature. The two assumptions of classical beam theory, that there is no shear component and that the beam deformation is continuous, are both investigated in this research.

The image provided in Figure 4 illustrates the presence of shear in the drop-stitch inflatable panel under four-point loading. The first assumption of classical beam theory assumes that there is no shear component, and therefore that the cross-sections of the beam remain perpendicular to the midplane of the beam (Budynas and Nisbett, 2011). Figure 4 illustrates through the use of markings that the cross-sections of the beam do not remain perpendicular, therefore indicating the presence of shear in the panel.

Figure 4. Example Demonstrating Shear in Four-Point Panel Deflection through Markings Along Center Plane (Half of Panel Shown)

The force-deflection curve for a drop-stitch inflatable structure under four-point bending is provided as an example in Figure 5. These curves demonstrate the dramatic pressure dependence of the panel stiffness on pressure. Note that the stiffness of the beam appears to increase with increase in internal pressure. Also note that the beam deflects with near constant load toward the end of the loading cycle for each case. Modeling the panel as a hollow thin-walled structure using classical beam theory equations does not predict the observed pressure dependence (Budynas and Nisbett, 2011). Current modeling methods assume that the properties of the panel skin material are pressure dependent and assume constant properties at discrete internal pressure values (Cavallaro et al., 2013; Felicissimo, 2015). This research seeks to model the pressure dependency through the inclusion of mechanisms, such as panel kinking due to local deformation, at the load points.

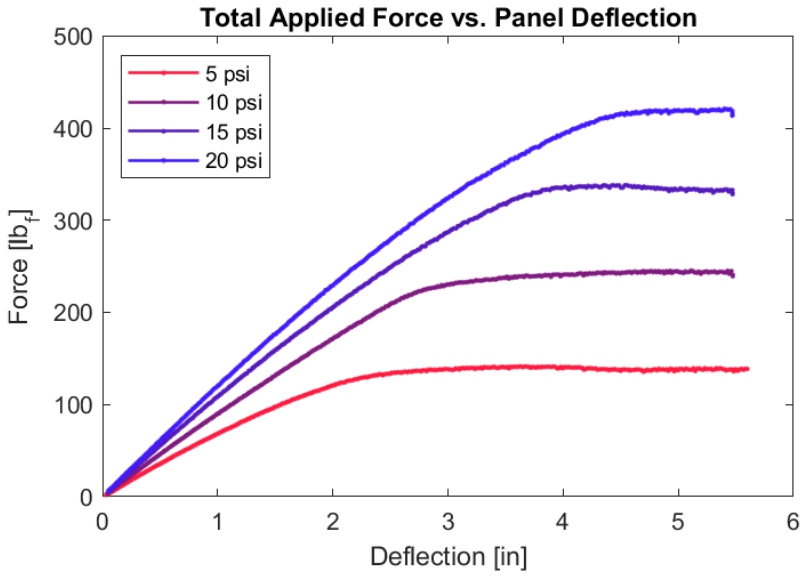

Figure 5. Force-Deflection Curve for Inflatable Drop-Stitch Panel under Four-Point Bending

1.3 Objective

The objective of this research is therefore to evaluate the validity of using Euler-Bernoulli beam theory for inflatable drop-stitch structures through the evaluation of panel material properties and panel performance under bending at varying inflation pressures.

Another objective of this research is to generate and analyze material data pertaining to the drop-stitch inflatable structures and the skin material of said structures for future use in inflatable panel models, including the use of composite-laminate theory and the development of detailed finite element models of the panels.

1.4 Methodology

This research aims to evaluate the response of panel skin material and the individual components of said skin material. The properties derived from the re-

sponse of the material can be applied to panel deflection models and compared to experimental inflatable panel bending results using the models discussed previously. Experimental data of real materials used in drop-stitch inflatable structures is therefore required in order to develop more accurate models of such structures.

1.4.1 Tensile Testing Overview

Material testing is inherently the most reliable way to predict the behavior of solids, and thus this thesis seeks to characterize the behavior of the panel skin using tensile testing methods. The tensile test is a method by which a specimen is subjected to an axial load P and any changes in the specimen length L are observed with respect to either time or load rate. The change in length with respect to the initial length of the specimen L_0 is denoted as δ. Stress σ_{yy} is defined as the force applied over a certain cross-sectional area of an object. For a bar under uniaxial loading in a tensile test, the applied nominal stress is simply calculated by Equation 1.4.1, where P is the applied load and A_0 is the original cross-sectional area of the bar. The strain ϵ_{yy} of the bar may then be defined as the ratio of elongation to the original length caused by the applied stress. The general equation for strain of a bar under uniaxial tension is provided in Equation 1.4.2, where L is the current length, L_0 is the initial length, and ΔL is the elongation.

$$\sigma_{yy} = \frac{P}{A_0} \tag{1.4.1}$$

$$\epsilon_{yy} = \frac{L - L_0}{L_0} = \frac{\Delta L}{L_0} \tag{1.4.2}$$

Using the generalized Hooke's Law provided in Equation 1.4.3, where σ_{xx} and σ_{zz} are the stresses in the x and z directions, and ν is Poisson's ratio, the elastic modulus E may be determined. Note that for uniaxial tension, $\sigma_{xx} = \sigma_{zz} = 0$ (Kelly, 2015). Also note that this relationship is only valid for linear-elastic materials prior to yielding, or for materials behaving in a locally linear-elastic

manner for small strains. The Poisson's ratio is defined as the negative ratio between the axial and transverse strain, $\nu = -\frac{\epsilon_{xx}}{\epsilon_{yy}}$.

$$E \cdot \epsilon_{yy} = \sigma_{yy} - \nu(\sigma_{xx} + \sigma_{zz}) \tag{1.4.3}$$

Using experimental digital image correlation techniques, the elongation of the sample in the y-direction and the contraction of the sample in the x-direction may be simultaneously measured in a non-invasive manner, allowing for the calculation of the strains in the x-direction ϵ_{xx}, the y-direction ϵ_{yy}, and the shear strain γ_{xy}. Note that for the uniaxial tension test, the applied load is normal to the cross-section and the shear strain is expected to be zero. Poisson's ratio may be estimated using the transverse strain ϵ_{xx}.

1.4.2 Directional Material Properties

An isotropic material is defined as a material for which the material response is unaffected by rigid body rotations of the reference configuration (Kelly, 2015). An anisotropic material is conversely any material of which the material properties are directionally dependent. The generalized Hooke's law provided in Equation 1.4.3 may be generalized further using matrices, as in Equation 1.4.4. The constants C_{ij} comprise the stiffness matrix for the material (Kelly, 2015). The stiffness matrix C_{ij} simplifies to Equation 1.4.5 for an isotropic, linear-elastic material.

$$\begin{bmatrix} \sigma_{xx} \\ \sigma_{yy} \\ \sigma_{zz} \\ \tau_{yz} \\ \tau_{xz} \\ \tau_{xy} \end{bmatrix} = \begin{bmatrix} C_{11} & C_{12} & C_{13} & C_{14} & C_{15} & C_{16} \\ C_{21} & C_{22} & C_{23} & C_{24} & C_{25} & C_{26} \\ C_{31} & C_{32} & C_{33} & C_{34} & C_{35} & C_{36} \\ C_{41} & C_{42} & C_{43} & C_{44} & C_{45} & C_{46} \\ C_{51} & C_{52} & C_{53} & C_{54} & C_{55} & C_{56} \\ C_{61} & C_{62} & C_{63} & C_{64} & C_{65} & C_{66} \end{bmatrix} \begin{bmatrix} \epsilon_{xx} \\ \epsilon_{yy} \\ \epsilon_{zz} \\ \gamma_{yz} \\ \gamma_{xz} \\ \gamma_{xy} \end{bmatrix} \tag{1.4.4}$$

$$\begin{bmatrix}\sigma_{xx}\\ \sigma_{yy}\\ \sigma_{zz}\\ \tau_{yz}\\ \tau_{xz}\\ \tau_{xy}\end{bmatrix} = \begin{bmatrix}\frac{1}{E} & \frac{-\nu}{E} & \frac{-\nu}{E} & 0 & 0 & 0\\ \frac{-\nu}{E} & \frac{1}{E} & \frac{-\nu}{E} & 0 & 0 & 0\\ \frac{-\nu}{E} & \frac{-\nu}{E} & \frac{1}{E} & 0 & 0 & 0\\ 0 & 0 & 0 & \frac{1}{2G} & 0 & 0\\ 0 & 0 & 0 & 0 & \frac{1}{2G} & 0\\ 0 & 0 & 0 & 0 & 0 & \frac{1}{2G}\end{bmatrix} \begin{bmatrix}\epsilon_{xx}\\ \epsilon_{yy}\\ \epsilon_{zz}\\ \gamma_{yz}\\ \gamma_{xz}\\ \gamma_{xy}\end{bmatrix} \tag{1.4.5}$$

A truly anisotropic is very difficult to characterize due to the sheer number of elastic constants. Materials that are not fully anisotropic are able to simplify Equation 1.4.4 based on material symmetries, such as how an isotropic material simplifies the equation due to its infinite number of symmetric planes. An orthotropic material is a special case of an anisotropic material in which the material properties are different on three mutually orthogonal axes and two planes of symmetry (Roylance, 2008). Equation 1.4.4 therefore simplifies into Equation 1.4.6 for orthotropic materials. For the two-dimensional fields analyzed through this research, this simplifies further into Equation 1.4.7. Note again that this only applies for linear elastic materials, or materials which are being approximated as linear elastic.

$$\begin{bmatrix}\sigma_{xx}\\ \sigma_{yy}\\ \sigma_{zz}\\ \tau_{yz}\\ \tau_{xz}\\ \tau_{xy}\end{bmatrix} = \begin{bmatrix}\frac{1}{E_1} & \frac{-\nu_{21}}{E_2} & \frac{-\nu_{31}}{E_3} & 0 & 0 & 0\\ \frac{-\nu_{12}}{E_1} & \frac{1}{E_2} & \frac{-\nu_{32}}{E_3} & 0 & 0 & 0\\ \frac{-\nu_{13}}{E_1} & \frac{-\nu_{23}}{E_2} & \frac{1}{E_3} & 0 & 0 & 0\\ 0 & 0 & 0 & \frac{1}{2G_{23}} & 0 & 0\\ 0 & 0 & 0 & 0 & \frac{1}{2G_{13}} & 0\\ 0 & 0 & 0 & 0 & 0 & \frac{1}{2G_{12}}\end{bmatrix} \begin{bmatrix}\epsilon_{xx}\\ \epsilon_{yy}\\ \epsilon_{zz}\\ \gamma_{yz}\\ \gamma_{xz}\\ \gamma_{xy}\end{bmatrix} \tag{1.4.6}$$

$$\begin{bmatrix}\sigma_{xx}\\ \sigma_{yy}\\ \tau_{xy}\end{bmatrix} = \begin{bmatrix}\frac{1}{E_1} & \frac{-\nu_{21}}{E_2} & 0\\ \frac{-\nu_{12}}{E_1} & \frac{1}{E_2} & 0\\ 0 & 0 & \frac{1}{2G_{12}}\end{bmatrix} \begin{bmatrix}\epsilon_{xx}\\ \epsilon_{yy}\\ \gamma_{xy}\end{bmatrix} \tag{1.4.7}$$

1.4.3 Panel Skin Material

The skin material for the drop-stitch inflatable woven panel is a fiber reinforced composite material. A fiber reinforced composite material is a material

with properties designed or altered by the addition of a fibrous material. In the case of the drop-stitch inflatable panels, the skin material is comprised of four primary layers: A coating of neoprene, a chafer layer, a secondary coating of neoprene, and the drop-stitch fabric layer. The configuration of these layers of the skin is illustrated in Figure 6.

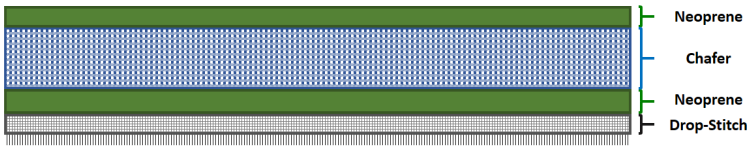

Figure 6. Layered Approximation of Drop-Stitch Inflatable Panel Skin

The analysis in this research assumes that the skin material is an orthotropic composite-laminate. Composite-laminate materials are materials composed of material layers of specified orientations, typically consisting of fibrous orthotropic materials (Roylance, 2010). The panel skin layer exhibits different properties when loaded in the warp and weft directions. The warp and weft directions are defined as the longitudinal and transverse fiber directions, or 0° and 90° orientations respectively (Majumdar, 2014). This research therefore analyzes the mechanical properties and behavior of the nonlinear woven fabric skin material under uniaxial loading. The data generated for this material and its constituent components will be used for the evaluation of panel bending models, as well as for use in future research into laminate models and detailed finite element models of the inflatable woven fabric drop-stitch structures.

1.5 Thesis Outline

The purpose of this thesis is to analyze the response of the orthotropic panel skin material and its constituent components utilizing experimental digital image correlation methods in order to accurately capture and model the behavior of

drop-stitch inflatable structures.

Chapter 2 will review published articles and research relevant to the analysis of drop-stitch inflatable woven structures, including design methods for such structures.

Chapter 3 will evaluate the classical beam theory equations for a beam under four-point bending, which inherently assume that the inflatable panel may be treated as an Euler-Bernoulli beam. The classical result will then be expanded in order to account for the contribution of shear strain on the deflection of the panel, as well as a method to outline the importance of the local deformation of the panel about the load points through the addition of an empirical, pressure dependent parameter.

Chapter 4 focuses on the experimental apparatuses used throughout this research, including the hardware used for tensile testing of the skin layer and a discussion of the digital image correlation apparatuses utilized for the measurement of displacement and strain fields. Chapter 4 also discusses the data processing and analysis methods, including the process of translating output from the testing machine hardware and digital image correlation software into viable data, the calculation methods of additional material parameters, as well as methods of quality assurance.

Chapter 5 covers all of the experimental analysis and results obtained throughout this research, both for the uniaxial tension testing of the skin material and its components as well as the comparison of experimental inflatable panel bend tests with the models discussed in Chapter 3.

Chapter 6 provides a summary of the relevant information and conclusions from each chapter, as well as a discussion of the potential for future research and experimentation.

CHAPTER 2

Literature Review

2.1 Inflatable Panel Beam Models

A model for the mechanics and behavior of drop-stitch inflatable fabric structures under four-point bending has previously been investigated by Cavallaro et al. (Cavallaro et al., 2013) using such techniques as shear-deformable beam theory (SDBT) in order to more accurately account for the shearing deformations found in inflatable structures subjected to four-point bending. The nonlinearity of the woven fabric skin layer poses challenges to the development of accurate beam bending models. These models rely on developing effective elastic and shear moduli for the composite woven fabric skin, arguing that since the properties of the skin are invariant that the change of stiffness in an inflatable panel is due to a pressure-dependent effective shear modulus, G_{eff}. A simplified approximation of an effective elastic modulus for the inflatable was similarly investigated by DiGiovanna (DiGiovanna, 2013).

The mechanical properties of the drop-stitch fabric panels have also been investigated by Felicissimo (Felicissimo, 2015). Felicissimo directly investigated the elastic modulus of the inflatable panel skin material as well as an effective elastic and shear modulus for a scaled version of the inflatable panels. The research by Felicissimo focused primarily on the effective moduli and loading characteristics of fully assembled parabeams rather than the skin material alone or its constituent components.

The properties investigated in the paper by Cavallaro et al., DiGiovanna, and Felicissimo are similar to that of this research, however this research aims to compare results through different methodologies and evaluate the assumptions concerning the skin material and the panel behavior used in this article. This paper

seeks to explain the behavior of the panel under bending through analysis of the skin properties rather than approximating the behavior using pressure dependent properties.

Falls and Waters (Falls and Waters, 2011) sought to investigate the accuracy of classical beam theory analysis for drop-stitch inflatable structures. The accuracy of the model was tested for panels between 250mm and 1000mm (9.84 in and 39.37 in) length, 100mm and 200mm (3.93 in and 7.87 in) thickness, and pressures between 21kPa and 103kPa (3.04 psi and 14.94 psi). The results of Falls and Waters demonstrate that the the classical beam theory model is not sufficient for modeling the behavior of drop-stitch inflatable panels. The results also demonstrate hysteresis in the panel. The panel investigated through this research has therefore been preconditioned in order to better capture the panel behavior in real-world applications.

2.2 Additional Panel Research

Additional modeling of the drop-stitch inflatable structure panels modal response has been addressed by Hulton et al. (Hulton et al., 2017). The research done by Hulton et al. addressed the finite element modeling of the drop-stitch panel while pressurized and subsequently analyzed the vibration response of the panel. The modal analysis of the panel demonstrated the importance of accounting for the nonlinear, hyperelastic behavior of the panel. The finite element model for the panel used by Hulton et al. also provides a principal stress of approximately 508 psi maximum, 447 psi average for the panel skin under inflation of 20 psi. Having this baseline stress for an inflated, unloaded panel is useful in interpreting the experimental results in Chapter 5.

2.3 Panel Skin Material Research

The behavior of the skin layer itself has similarly been investigated by Cavallaro et al. (Cavallaro et al., 2007), in which the contributions of shear stress within woven fabric panels is addressed through finite element modeling of the woven fabric and experimental validation. Similar analysis done prior to the work of Cavallaro et al. for space applications, such as done by Main et al. (Main et al., 1994) in the analysis of woven fabric structures for space applications, analyzed the woven fabrics without regards to the contributions of shear on the fabric structures. Cavallaro et al. proceeded to test the shear contribution in the fabric panels under biaxial tension and in-plane shear. This research aims to build upon this research and investigate the mechanical properties of the combined neoprene and woven-fabric skin under applied stress.

A more general investigation of nylon woven fabrics embedded in neoprene was accomplished by Aboshio et al. (Aboshio et al., 2015). The mechanical behavior of neoprene-coated nylon woven fabric composites was assessed using both uniaxial and biaxial loading conditions under controlled environmental circumstances. This research was done in order to fit hyperelastic models to the generated uniaxial and biaxial data. The hyperelastic models could then be used to model the material behavior in complex geometries and applications. The research done by Aboshio et al. verifies that the skin material for this panel may require hyperelastic models in order to accurately capture the behavior of the material, but also verifies the quasi-linear elastic behavior of such materials at low strains.

CHAPTER 3

Inflatable Panel Modeling

Models currently used for drop-stitch inflatable structures assume that properties such as the elastic modulus or the shear modulus of the panel vary with pressure (Cavallaro et al., 2013). The effective property at a given inflation pressure is then applied to Euler-Bernoulli beam theory. The model investigated through this research assumes that the properties of the skin material, which are independent of internal pressure, are to be used in computing beam properties. The two major assumptions of Euler-Bernoulli beam theory are evaluated through analyzing the shear contributions to the deflection of the beam and allowing kinking of the panel through local deformation at the load points.

This chapter will discuss the modeling of the inflatable drop-stitch structure under four-point bending. The classical solution for the deflection of a panel under four-point bending will first be considered, including the definition of the panel loading and the moment of inertia of the panel. The proposed shear strain contribution to the deflection of the panel and the effect of kinking on the deflection will each then be derived for the inflatable drop-stitch panels.

3.1 Four-Point Bending from Beam Theory

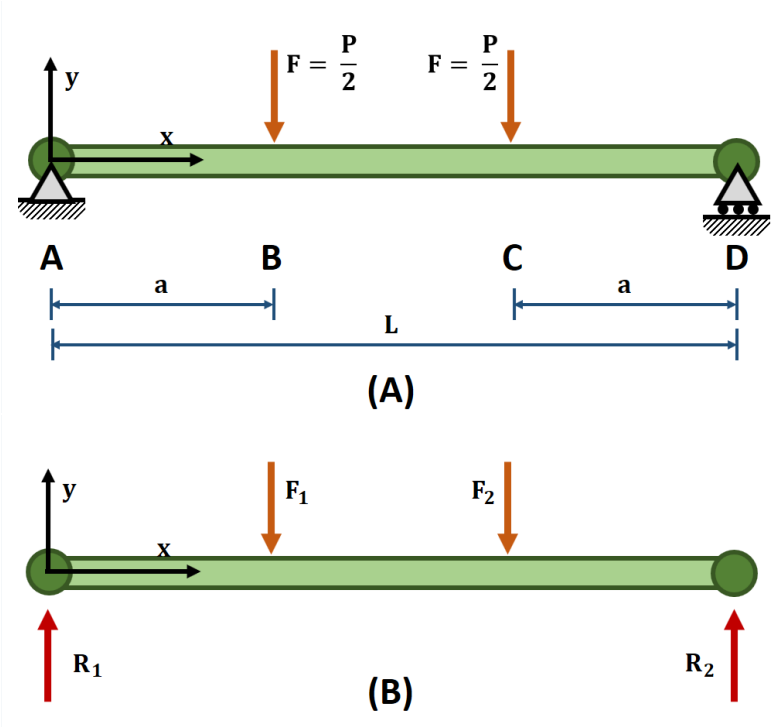

Figure 7. Four-Point Bending Loading Diagram (A) and Equivalent Free-Body Diagram (B)

A four-point bending test of a drop-stitch inflatable fabric structure is able to characterize the performance of the Euler-Bernoulli model by analyzing the deflection of the panel. A free body diagram of a four-point bend test is provided in Figure 7. Note that regions AB and CD are between the supports and the loading points, and region BC is the region between the loading points.

Equations 3.1.1 and 3.1.2 are the equations for the four-point bending deflection of the midplane of an Euler-Bernoulli beam. Equation 3.1.1 characterizes the deflection of the AB region while Equation 3.1.2 characterizes the deflection of the BC region. Region CD is not included, as region CD is a mirror of region AB. The maximum absolute deflection of the beam under four-point bending is found at the midpoint between the two supports, and is calculated by Equation 3.1.3

(Collins et al., 2010).

$$y_{AB}(x) = \frac{Fx}{6EI}(x^2 + 3a^2 - 3La) \tag{3.1.1}$$

$$y_{BC}(x) = \frac{Fa}{6EI}(3x^2 + a^2 - 3Lx) \tag{3.1.2}$$

$$y_{max} = \frac{Fa}{24EI}(4a^2 - 3l^2) \tag{3.1.3}$$

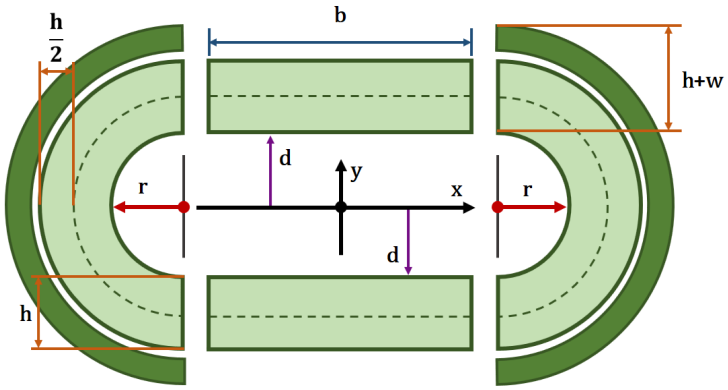

Figure 8. Semicircular and Rectangular Sectioning used to Estimate the Area Moment of Inertia

The area moment of inertia for the panel is required in order to calculate its deflection under loading. Figure 8 demonstrates the composite shapes used to estimate the area moment of inertia of the inflatable panel. Note that the composite shape is comprised of two parallel rectangular sections and two semicircular sections on either end of the cross-section. Also note that h is the thickness of the panel skin, b is the length of the flat portion of the panel, d is the distance from the inner wall of the flat portion of the panel to the x-axis, r is the inner radius of the sidewall, and w is the thickness of the second layer added to the outer surface of the sidewalls. For the purpose of this analysis, $d = r$ and $w = h$.

Using Parallel Axis Theorem relative to the x-axis shown in Figure 8, the area moment of inertia for one of the rectangular and semicircular components can be expressed using Equation 3.1.5 and Equation 3.1.4, respectively

(Collins et al., 2010). Combining the components using Equation 3.1.6, the estimated area moment of inertia for the inflatable structure is found to be Equation 3.1.7.

$$I_{x,semi} = \frac{\pi}{8}\Big[(r+h+w)^4 - r^4\Big] \tag{3.1.4}$$

$$I_{x,rect} = \frac{bh^3}{12} + bh(d+\frac{h}{2})^2 \tag{3.1.5}$$

$$I_x = 2I_{x,rect} + 2I_{x,semi} \tag{3.1.6}$$

$$I_x = 2\Big[\frac{bh^3}{12} + bh(d+\frac{h}{2})^2\Big] + \frac{\pi}{4}\Big[(r+2h)^4 - r^4\Big] \tag{3.1.7}$$

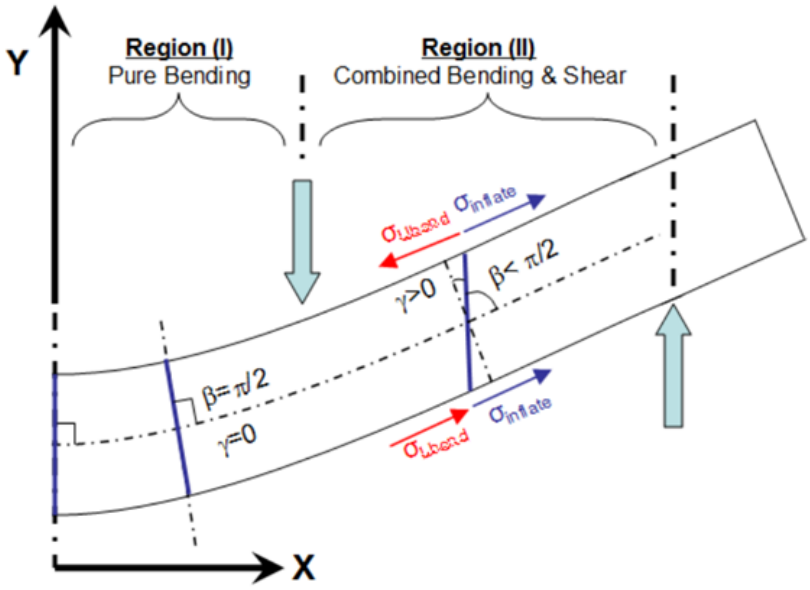

Figure 9. Shear Deformation under Four-Point Loading (Cavallaro et al., 2013)

The classical beam theory equations referenced thus far assume that the drop-stitch inflatable panel is able to be considered an Euler-Bernoulli beam. It is also important to consider local deformation in the vicinity of the load points and the shear deformation in the side-walls for the drop-stitch inflatable panels. The cross-sections of the panel cannot be assumed to remain normal to the deformed axis of the panel due to the presence of shear stresses (Ho, 2015). Cavallaro et al. provided Figure 9 to demonstrate the shear deformation found in the drop-stitch

inflatable panel loading. Note that in Figure 9 $\sigma_{inflate}$ represents the pretension due to inflation and σ_{Ubend} represents the stress due to the four-point bend. Also note that the pretension stress and bending stress oppose each other on the top layer of the panel and are superimposed on the bottom layer.

3.2 Shear Strain Contribution

The contribution of shear strain on the deflection of the beam is calculated using strain energy methods. The reaction forces R_1 and R_2 are first found through global equilibrium of Figure 7, resulting to be Equations 3.2.1 and 3.2.2.

$$R_1 = (1 - \frac{a}{L})F_1 + \frac{a}{L}F_2 \tag{3.2.1}$$

$$R_2 = \frac{a}{L}F_1 + (1 - \frac{a}{L})F_2 \tag{3.2.2}$$

The shear force distribution along the length of the panel $V(x)$ is then characterized through the piecewise Equation 3.2.3. Note that in Equation 3.2.3, $\alpha = \frac{a}{L}$ and $\beta = 1 - \frac{a}{L}$.

$$V(x) = \begin{cases} -\beta F_1 - \alpha F_2 & 0 < x \leq a \\ \beta(F_1 - F_2) & a < x \leq L - a \\ \alpha F_1 + \beta F_2 & x > L - a \end{cases} \tag{3.2.3}$$

The shear force distribution defined in Equation 3.2.3 may then be used in the calculation of strain energy. The strain energy due to direct shear is shown in Equation 3.2.4 (Budynas and Nisbett, 2011). $U_{shear}(x)$ is the strain energy due to direct shear, F is the applied shear load, A_{shear} is the cross-sectional area experiencing the shear strain, G is the shear modulus of the material, and C is a constant dependent on the cross-sectional geometry.

$$U_{shear}(x) = \int \frac{CV^2}{2A_{shear}G} dx = \frac{CV^2}{2A_{shear}G} \int dx \tag{3.2.4}$$

The cross-sectional area experiencing the shear strain in the inflatable panel is the combined area of the two semicircular sidewall sections shown in Figure 8. The cross-sectional area is approximated to be geometrically equivalent to a thin-walled cylinder, wherein the cross-sectionally dependent constant C is typically taken to be 2 (Budynas and Nisbett, 2011).

Since $\int_0^a = a$, $\int_a^{L-a} = L - 2a$, and $\int_{L-a}^{L} = a$, and substituting appropriate equations from Equation 3.2.3 for $V(x)$, Equation 3.2.4 is evaluated to be Equation 3.2.5.

$$U = \frac{C}{2A_{shear}G}[a(\beta F_1 + \alpha F_2)^2 + (L-a)\beta^2(F_1 - F_2)^2 + a(\alpha F_1 + \beta F_2)^2] \tag{3.2.5}$$

The contribution of the shear strain on the deflection of the panel is determined using Castigliano's Theorem. The general form of Castigliano's Theorem for linear displacement is provided in Equation 3.2.6 (Budynas and Nisbett, 2011).

$$\delta_i = \frac{\partial U}{\partial F_i} \tag{3.2.6}$$

Where δ_i is the displacement in the direction i, U is the strain energy, and F_i is the load applied in the i direction. Applying Castigliano's theorem at $x = a$ yields Equation 3.2.8. Setting $F_1 = F_2 = F = \frac{P}{2}$ yields

$$\delta_{x=a} = \frac{\partial U}{\partial F_1} = \tag{3.2.7}$$

$$= \frac{C}{A_{shear}G}[a\beta(\beta F_1 + \alpha F_2) + (L-a)\beta^2(F_1 - F_2) + a\alpha(\alpha F_1 + \beta F_2)] \tag{3.2.8}$$

$$\delta_{x=a} = \frac{CPa}{2A_{shear}G} \tag{3.2.9}$$

Applying this result throughout regions AB, BC, and CD with the constant $C = 2$ for a thin-walled tube (Budynas and Nisbett, 2011) yields the piecewise equation for deflection due to shear strain, Equation 3.2.10.

$$y_\tau(x) = \begin{cases} \frac{CPx}{2A_{shear}G} & 0 < x \leq a \\ \frac{CPa}{2A_{shear}G} & a < x \leq L - a \\ \frac{CP(L-x)}{2A_{shear}G} & x > L - a \end{cases} \tag{3.2.10}$$

Note that for region AB the shear contribution to the deflection has a constant negative slope and for the BC region the shear contribution is a constant displacement. The CD region is a mirror of the displacement for the AB region about the centerpoint of the span, $x_{center} = \frac{L}{2}$.

3.3 Beam Theory with Local Deformation

A modification of the classical beam theory equations are derived in order to account for the kinking of the beam at the load points due to local deformation. The classical beam theory solution may be modified in order to account for the local deformations of the inflatable panel by introducing a difference in the slope at the loading points. The angular discontinuity variable is denoted as θ in this analysis. The deflection of the inflatable structure with an included discontinuous term θ is accomplished using traditional beam theory relationships. Assuming that the deflection is of the general form Equation 3.3.1, the first and second derivatives may be evaluated as Equations 3.3.2 and 3.3.3, respectively. Equation 3.3.3 is equated to $\frac{M}{EI}$ in order to determine $a_1 = \frac{P}{12EI}, a_2 = 0$. The moment in the panel for region AB varies linearly with x through the equation $M = \frac{Px}{2}$. The variable a_0 may then also be determined by noting that the deflection at the support must be zero, and thus $a_4 = 0$, as is shown in Equation 3.3.4.

$$y_{AB}(x) = a_1x^3 + a_2x^2 + a_3x + a_4 \tag{3.3.1}$$

$$y'_{AB}(x) = 3a_1x^2 + 2a_2x + a_3 \tag{3.3.2}$$

$$y''_{AB}(x) = 6a_1x + 2a_2 = \frac{M}{EI} = \frac{Px}{2EI} \rightarrow a_1 = \frac{P}{12EI}, a_2 = 0 \tag{3.3.3}$$

$$y_{AB}(0) = a_4 = 0 \rightarrow a_4 = 0 \tag{3.3.4}$$

Repeating a similar process for region BC, wherein the moment in the panel is a constant $M = \frac{Pa}{2}$ results in Equations 3.3.5 through 3.3.8. Note that Equation 3.3.8 is evaluated at the boundary condition that the derivative of the deflection must be zero at the horizontal midpoint of the panel.

$$y_{BC}(x) = b_1x^3 + b_2x^2 + b_3x + b_4 \tag{3.3.5}$$

$$y'_{BC}(x) = 3b_1x^2 + 2b_2x + b_3 \tag{3.3.6}$$

$$y''_{BC}(x) = 6b_1x + 2b_2 = \frac{M}{EI} = \frac{Pa}{2EI} \rightarrow b_1 = 0, b_2 = \frac{Pa}{4EI} \tag{3.3.7}$$

$$y'_{BC}(\frac{L}{2}) = \frac{PaL}{4EI} + b_3 = 0 \rightarrow b_3 = -\frac{PaL}{4EI} \tag{3.3.8}$$

The discontinuity variable θ is then introduced at the load point B using Equation 3.3.9. The derivation of the parameters b_1, b_2, b_3 are required in order to evaluate 3.3.9.

$$y'_{AB}(a) = y'_{BC,\theta}(a) + \theta \tag{3.3.9}$$

$$3a_1x^2 + 2a_2x + a_3 = 3b_1x^2 + 2b_2x + b_3 \tag{3.3.10}$$

$$\frac{P}{4EI}a^2 + a_3 = 2\Big(\frac{Pa}{4EI}\Big)a - \frac{PLa}{4EI} + \theta \rightarrow a_3 = \frac{Pa}{4EI}(a - L) - \theta \tag{3.3.11}$$

The discontinuity variable must then be accounted for again by including θ at load point C, as shown in Equation 3.3.12. The value of b_4 may then be determined by equating Equation 3.3.1 and Equation 3.3.5 at point $x = a$. The solved value for b_4 is provided in Equation 3.3.14.

$$y_{AC}(a) = y_{BC,\theta}(a) + \theta \tag{3.3.12}$$

$$a_1x^3 + a_2x^2 + a_3x + a_4 = b_1x^3 + b_2x^2 + b_3x + b_4 \tag{3.3.13}$$

$$b_4 = a_1a^3 - b_2a^2 + (a_3 - b_3)a \rightarrow b_4 = \frac{Pa^3}{12EI} - a\theta \tag{3.3.14}$$

Recalculating the deflection of the inflatable structure under four-point bending with the additional term θ results in Equations 3.3.15 and 3.3.16 for the deflection of the panel.

$$y_{AB}(x) = \frac{P}{12EI}x^3 + \Big[\frac{P}{4EI}(a^2 - aL) - \theta\Big]x \tag{3.3.15}$$

$$y_{BC}(x) = \frac{Pa}{12EI}(3x^2 - 3Lx + a^2) - a\theta \tag{3.3.16}$$

Note that deflection $y_CD(x)$ is a mirror of deflection $y_AB(x)$ about the center of the span. Through similar analysis y_{CD} may be written as shown in Equation 3.3.17. Writing the deflection results of the AB, BC, and CD regions as a piecewise function yields the deflection due to bending $y_b(x)$, as shown in Equation 3.3.18.

$$y_{CD}(x) = \frac{P}{12EI}(L - x)^3 + \Big[\frac{P}{4EI}(a^2 - aL) - \theta\Big](L - x) \tag{3.3.17}$$

$$y_b(x) = \begin{cases} \frac{P}{12EI}x^3 + \Big[\frac{P}{4EI}(a^2 - aL) - \theta\Big]x & 0 < x \leq a \\ \frac{Pa}{12EI}(3x^2 - 3Lx + a^2) - a\theta & a < x \leq L - a \\ \frac{P}{12EI}(L - x)^3 + \Big[\frac{P}{4EI}(a^2 - aL) - \theta\Big](L - x) & x > L - a \end{cases} \tag{3.3.18}$$

The deflections are then able to be added together by the principle of superposition (Ho, 2015), resulting in a combined equation for the total deflection of the inflatable panel, $y_{total}(x) = y_b(x) + y_\tau(x)$.

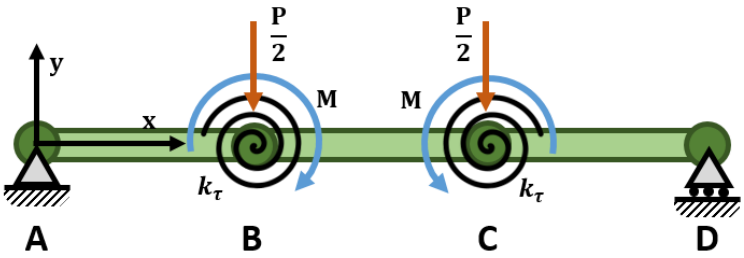

Figure 10. Approximate Torsional Stiffness Model for Panel Deflection

One method to characterize the behavior of the discontinuity model performance is a torsional stiffness k_τ. The torsional stiffness is used to characterize the resistance of the panel to the local deformation about the load point, as shown in the equivalent free body diagram Figure 10. This model treats the load points as hinges which resist bending due to torsional springs with torsional spring constant k_τ. This torsional stiffness is related to the angular discontinuity variable θ by Equation 3.3.19.

$$k_\tau = \frac{Fa}{\theta} = \frac{Pa}{2\theta} \tag{3.3.19}$$

CHAPTER 4

Experimental Methods

4.1 Tensile Testing

Tensile testing involves subjecting a specimen to an axial load and observing the change in state of the specimen. Traditionally the change of state observed is the change in length with respect to the change in applied load or with respect to time, as well as the lateral contraction as a function of applied load. The tensile test allows one to define the stress-strain relationships of the specimen which may be used in further engineering analysis or to aid in design decisions. A lateral contraction provides a measure of Poisson's ratio for linear elastic materials. In the case of this research, the tensile tests perform allow for the characterization of the mechanical behavior of the drop-stitch woven inflatable structure skin material, and allow for further nonlinear parameterization of its behavior.

4.1.1 Tensile Test Hardware

The hardware used in order to execute the uniaxial tensile tests are a Shimadzu EZ-LX Universal Testing Machine (UTM). The UTM allows for sample coupons to be mounted within the grips and pulled to the specified stroke or force at the specified rates. The load and stroke are measured through the UTM load cell and through the main column, respectively. The maximum load of the load cell used in these experiments was approximately 100 lb_f, as the information for large loads, strains, or at failure were not explicitly required for modeling within the operational range of the inflatable structures.

4.1.2 Tensile Sample Preparation

The samples analyzed must first be prepared for use in the uniaxial testing machine. Simple rectangular samples are chosen for these experiments. The dog-

bone samples typically used for metallic materials under uniaxial tension are not used for these experiments due to the continuous fibers within some of the materials tested. The use of rectangular samples allows for simpler sample preparation and a reduction in the risks associated with machining standard dog-bone samples from thin continuously fibrous materials or thin rubber materials. The sample dimensions were kept consistent for each material tested. The dimensions used per material are provided in Table 1. Note that the length is the grip-to-grip length of the sample.

Table 1. Dimensions of Uniaxial Tension Test Samples

Sample	**Length [in]**	**Width [in]**	**Thickness [in]**
Panel Skin	9.00	1.00	0.0550
Neoprene	8.50	1.00	0.0313
Chafer Layer	8.00	1.00	0.0200
Drop-Stitch Layer	8.00	1.00	0.0150

4.2 Digital Image Correlation (DIC)

This research aims to characterize the nonlinear behavior of the skin material using digital image correlation (DIC) techniques. DIC is a method by which two- or three-dimensional measurement of displacement or strain fields derive from sequential images of the loading cycle. DIC software tracks the movement of marked points on the surface through the sequence of photographs, thus generating the displacement field. The software subsequently derives the strain field from this information. The algorithm by which the DIC software used in this analysis, Ncorr2D, tracks points and calculates strain is documented by Blaber et al. (Blaber et al., 2015). The performance of Ncorr2D has been verified experimentally for use in solid mechanics at the Engineering Optics Laboratory in the India Institute of Technology (Harilal and Ramji, 2014).

The mechanical properties of the skin layer of the drop-stitch inflatable fabric structure are derived from the DIC technique on samples of the skin layer subjected to uniaxial and biaxial loading. The strains calculated using DIC analysis may be related back to the force and displacement measurements from the material testing systems by matching images of the loading cycle, as mentioned through the work of Justusson et al. (Justusson et al., 2013). The skin layer, again as shown in Figure 3, is a combination of the polymer neoprene and fabric. This research will therefore test the composite polymer-fabric skin as an entity, the polymer coating, and the chafer layer fabric individually in order to later characterize the mechanical contributions of the fabric portion of the skin for use in developing detailed finite element models of the inflatable woven fabric drop-stitch panels.

Two-dimensional DIC analysis is chosen for this research, rather than alternative three-dimensional analysis, as the out-of-plane deformation of the samples under uniaxial and biaxial tension testing is assumed to be negligible. Significant out-of-plane bending would require two mounted cameras focused on the same face of the sample in order to capture the three-dimensional deformation, however the sample material under the loading described is not expected to experience significant out-of-plane deformation, similar to the work by Justusson et al. (Justusson et al., 2013). Justusson et al. performed tensile tests upon fabric composites and compared strains calculated from two-dimensional DIC analysis on the samples and traditional strain gauges. The result of this investigation demonstrated that only two-dimensional DIC analysis is required for a single face of a tensile test sample, however for more accurate results a single camera on the front and back of the sample could be used. This research therefore utilizes two-dimensional DIC analysis for the measurement of planar displacement and strain fields while paying particular attention to verifying the accuracy of the results

generated through digital image correlation.

4.2.1 DIC Hardware

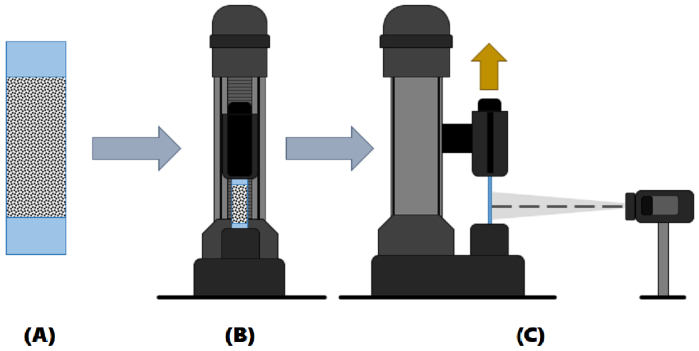

Figure 11. General Process for Using DIC for a Tensile Test; (A) Sample Preparation, (B) Mounting the Sample within Tensile Testing Machine, (C) Loading and Recording the Sample with Tensile Testing Machine and Camera

The equipment required for DIC analysis is a sufficiently high-resolution camera to capture the movement of the marked points, and the necessary camera rigging equipment, such as a camera mount or lighting elements. The uniaxial and biaxial testing of these samples are performed on a uniaxial and biaxial loading frame with a single camera fixed at a set distance perpendicular to the plane of loading (Justusson et al., 2013). The general process for setting up the tensile test with DIC is illustrated in Figure 11. Note that during the uniaxial tension test, images are taken by the camera at discrete time intervals in order to capture the state of the sample over the course of the loading. Note that an additional device is used in conjunction with the digital camera in order to take individual frames of the loading cycle at regular a regular time interval, dt. An example of the process outlined in Figure 11 is provided in Figure 12.

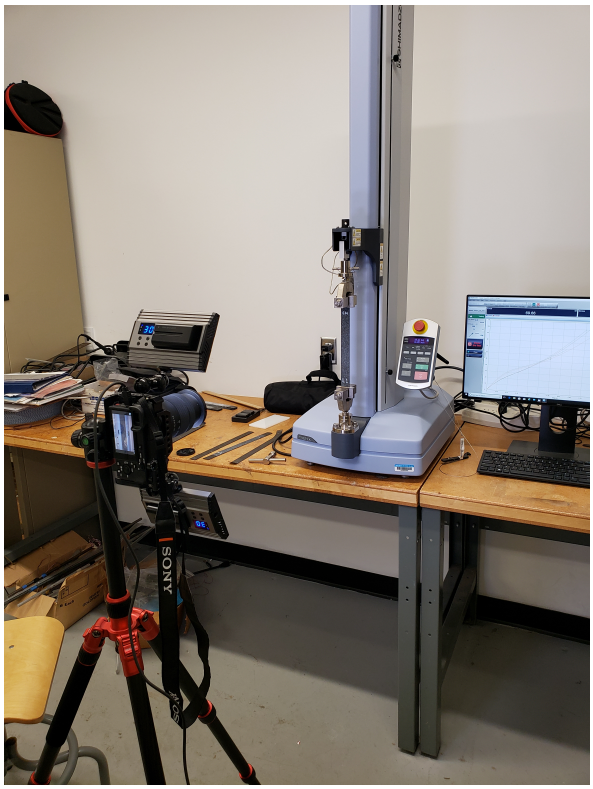

Figure 12. Example of DIC Experimental Hardware Setup

4.2.2 DIC Sample Preparation

The use of digital image correlation requires that the sample be marked by points on the surface facing the camera within the region of interest. A higher number of tracking points and a finer spread of points over the surface of the sample results in increased accuracy of the DIC measurement (Blaber et al., 2015). Samples were therefore prepared by misting spray paint over the surface of the samples in order to maximize point coverage and minimize the footprint of the ink on the samples in order to maximize effectiveness of the DIC processing.

4.2.3 DIC Software

As mentioned previously, the software used in order to execute the DIC analysis is Ncorr2D. Ncorr2D is an open-source two-dimensional DIC software developed in MATLAB by Dr. Justin Blaber. The inputs required by Ncorr2D are the im-

ages taken from the uniaxial tension test, the scale of the image in terms of unit measurement per pixel, and various design software parameters to specify how the software tracks and processes information. The images are formatted to the appropriate size, orientation, and monotonically increasing name scheme required for Ncorr2D using the MATLAB function provided in Appendix A. The output of the software includes the displacement fields and the three primary two-dimensional strain fields; the axial, lateral, and shear strains (Blaber et al., 2015). An example of the software interface for Ncorr2D is provided in Figure 13.

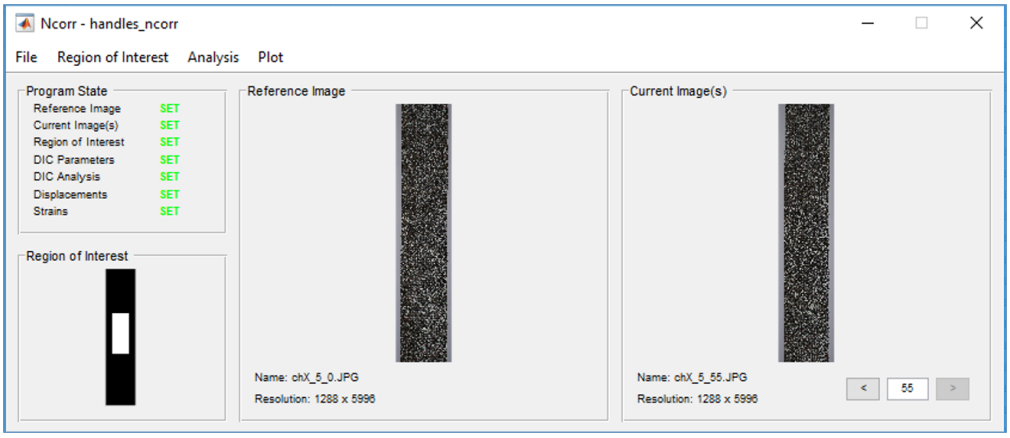

Figure 13. Example of Ncorr2D Interface

The output from Ncorr2D is saved to the MATLAB workspace within a structure file containing the displacement fields in the U and V directions for all frames, the normal strain fields ϵ_{xx} and ϵ_{yy} for all frames, the shear strain field γ_{xy} for all frames, and a record of the input parameters used in the analysis. In order to use the output information, the field matrices for each variable at each frame are reduced to single averaged values. The averaged values may then be synced with the force measurements from the tensile testing machine using the known time step between frames. The actual value of the force at the time the frame was taken is interpolated using linear interpolation at time $n \cdot dt$, where n is the frame number and dt is the time step between frames. The minimum possible time step

between frames for the hardware used in this experiment is one frame per second. Experiments in this research typically took one frame every two to four seconds. The time between measurements for the tensile testing machine used in this research is sufficiently frequent, approximately every 0.01 seconds, such that there is a minimal loss of accuracy in the mapping to the time steps of the frames. The averaging and time-syncing of the experimental data is accomplished using the MATLAB code provided in Appendix B.

4.3 Four-Point Panel Bending

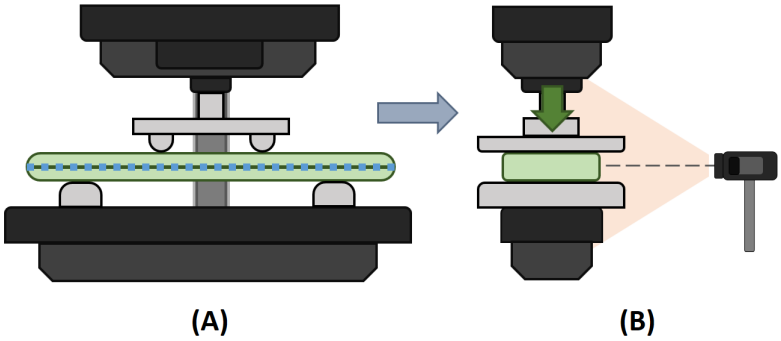

Figure 14. General Process for the Drop-Stitch Inflatable Panel Four-Point Bend Experiment; (A) Mounting the Sample within the MTS Frame, (B) Applying a Load to the Panel and Recording Deflection using a Camera

Table 2. Panel and Loading Configuration Dimensions

Name	Symbol	Value	Units
Span	l	76.00	in
Support to Load	a	26.00	in
Width	b	20.00	in
Skin Thickness	h	0.055	in
Sidewall Radius	r	2.000	in

4.3.1 Four-Point Bend Hardware

An MTS loading frame is used to execute the experimental four-point bend of the drop-stitch inflatable woven structure, deflecting the inflated beam by six

inches at the loadpoints B,C. Table 2 lists the loading and panel parameters for the experiment, as referenced in Figures 7 and 8.

The midplane deflection of the beam under this loading is determined by capturing pictures of the panel deflection at regular intervals during the loading cycle. Identifiable marked points along the beam are then able to be tracked using image processing functions within MATLAB, and from this tracking the deflection of the panel may be measured. A laser gauge is also mounted beneath the center of the panel in order to verify the deflection measured through the images. An overview of the panel mounting and tracking is shown in Figure 14.

4.3.2 Four-Point Bend Panel Tracking

The deflection of the panel under four-point bending is tracked using the marked points along the midplane. The MATLAB script in Appendix C binarizes the image of the panel bend and extracts the x and y coordinates of the marked points. An example of the experimental process of this tracking for a single frame is in Figure 15.

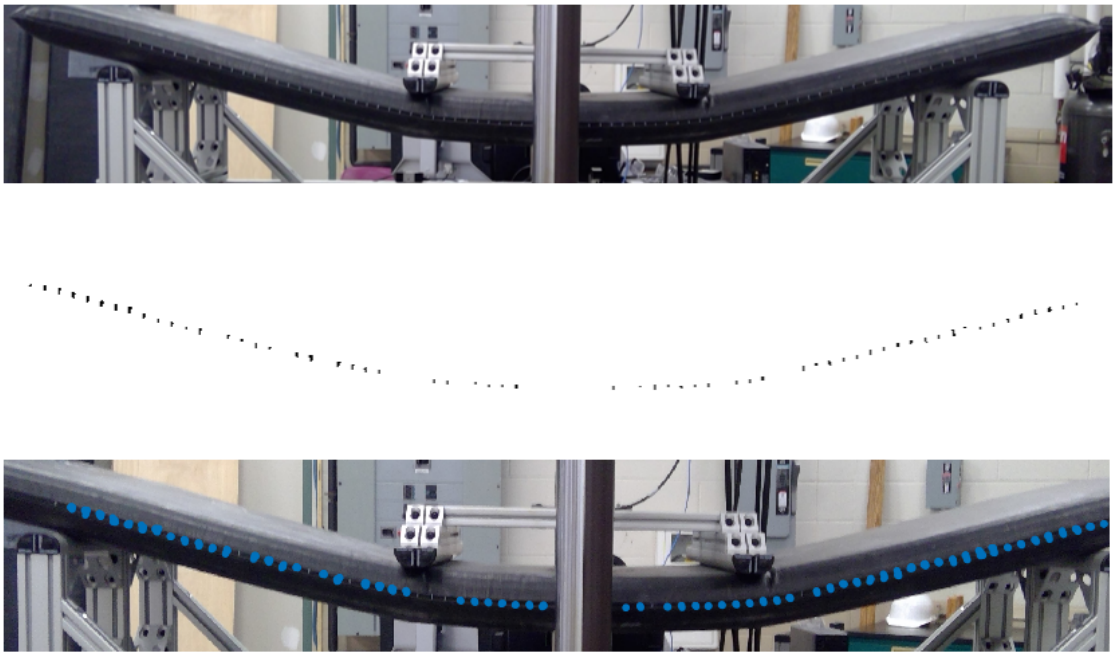

Figure 15. Original image from bend test (Top), Binary map of points along mid-plane of beam (Middle), Tracked points mapped back to original image (Bottom)

CHAPTER 5

Results

5.1 Panel Skin

The following uniaxial tensile data in Figures 16 through 19 are taken from samples for the panel skin cut in the weft and warp directions. The panel skin material is the combination of the chafer, neoprene, and drop-stitch layers as shown in Figure 6. The same two samples for weft and warp respectively have been tested repeatedly over multiple sessions in order to verify the properties of the material under repeated loading. Note that the cases denoted 1, 3, and 5 were the first loading cases per session for each of the following figures.

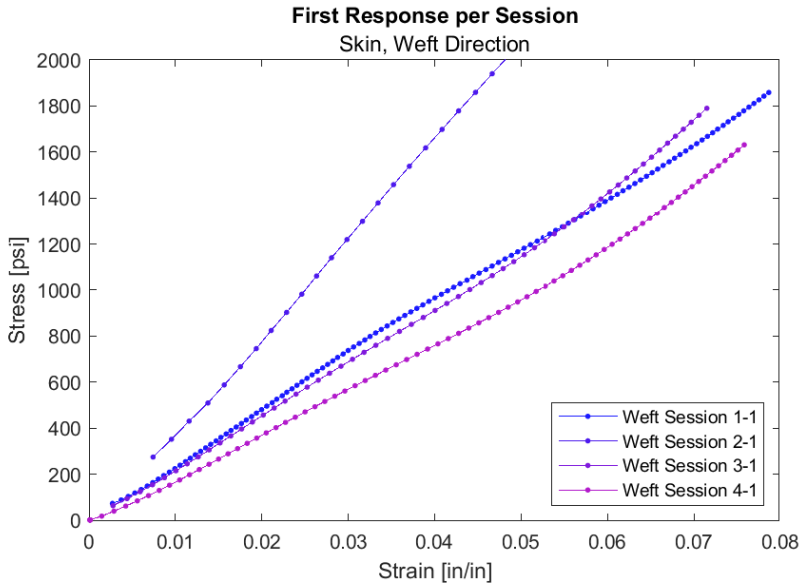

Figure 16. Stress-Strain Curve for Initial Loading of Skin Sample in the Weft Direction, Per Testing Session

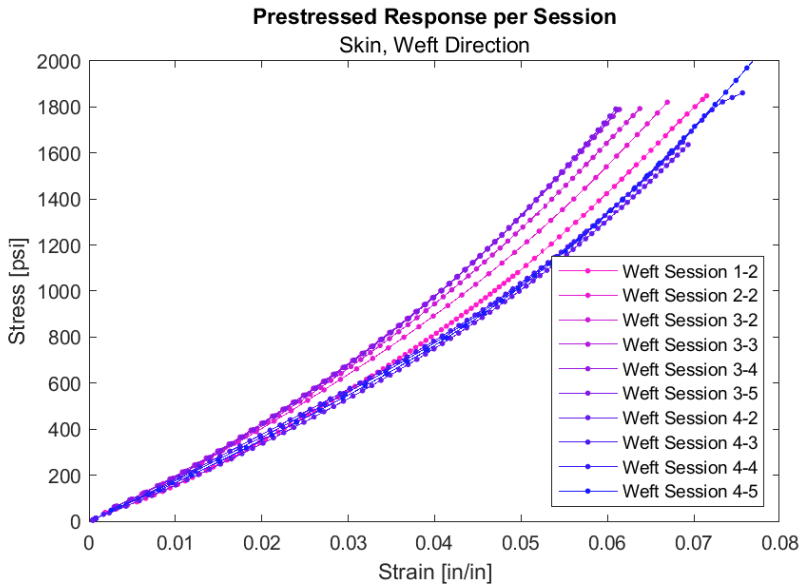

Figure 17. Stress-Strain Curve after Initial Loading for Skin Sample in the Weft Direction

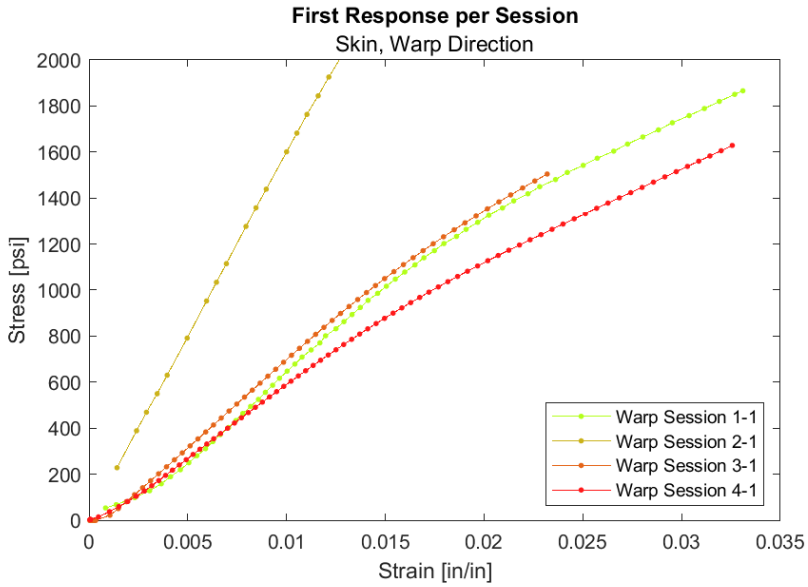

Figure 18. Stress-Strain Curve for Initial Loading of Skin Sample in the Warp Direction, Per Testing Session

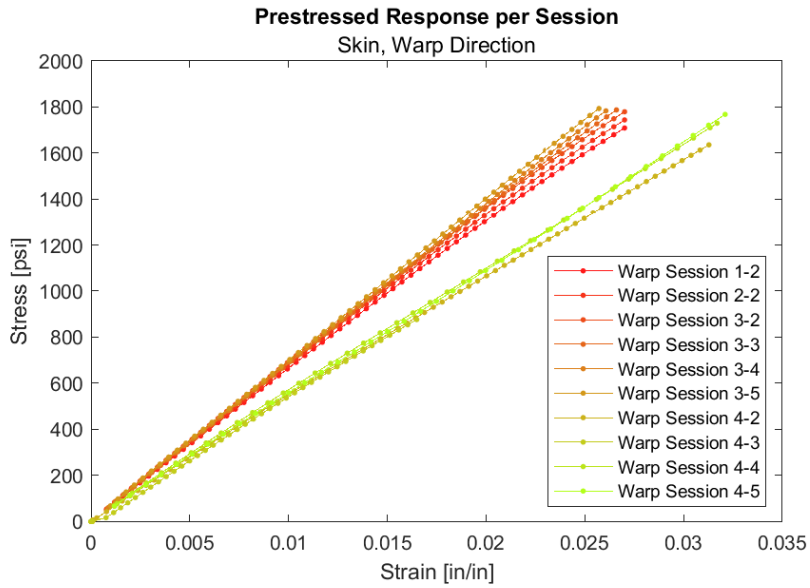

Figure 19. Stress-Strain Curve after Initial Loading for Skin Sample in the Warp Direction

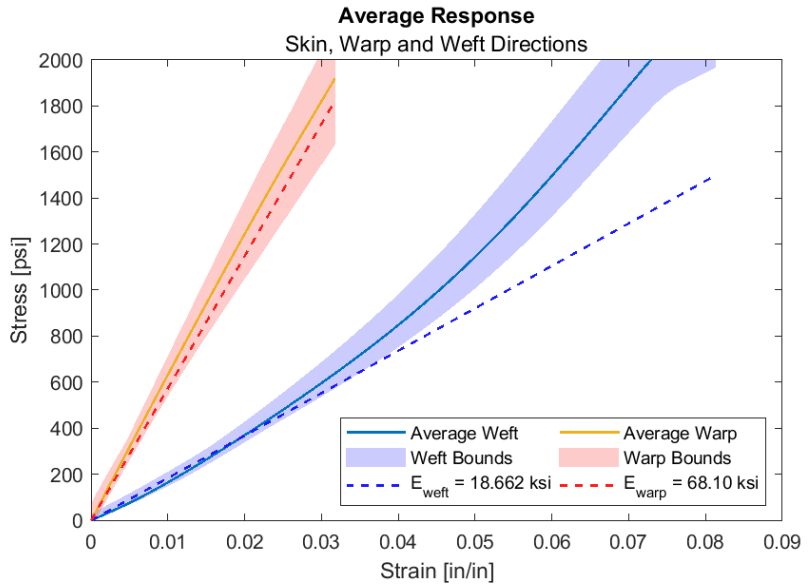

Figure 20. Average Stress-Strain Curve for Warp and Weft Directions of Skin Material, with marked Elastic Moduli

Figures 16 and 17 show the uniaxial tension results for the panel skin material

loaded in the weft direction. Similarly, Figures 18 and 19 show the uniaxial tension results for the panel skin material pulled in the warp direction. It should be noted that for both the warp and weft samples, the initial loading of the sample shown in Figures 16 and 18 yielded stress-strain responses significantly different in form than the stress-strain curves shown in Figures 17 and 19, which each demonstrated more consistent properties. One theory to explain this unusual behavior is that the fibers of the chafer layer within the skin sample are tightening under initial loading, and then relax between testing sessions.

Figure 20 shows the averaged, stress-strain response of the panel skin and the effective elastic moduli for the weft and warp directions, respectively. The initial loading per session is excluded from the calculation of the elastic moduli. The weft direction elastic modulus is approximately 18.66 ksi, while the warp direction elastic modulus is approximately 68.10 ksi.

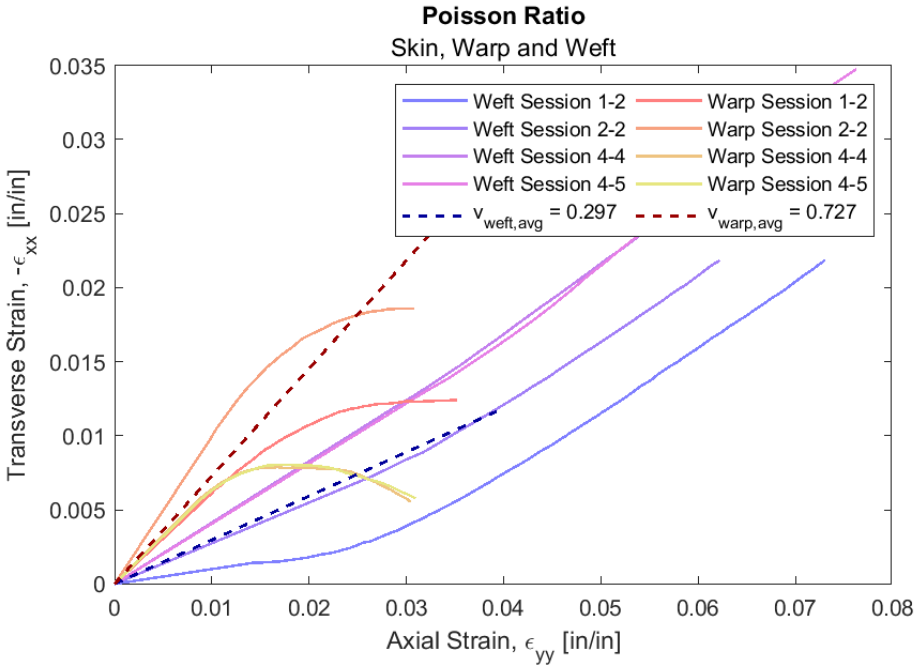

Figure 21. Estimation of Poisson Ratio for Warp and Weft Directions

Figure 21 demonstrates the calculation of Poisson's ratio from the axial and lateral strains determined through DIC. The determination of the Poisson ratio for the skin material is more complex than for typical materials due to the interaction of the layered components of the skin with each other, and the weave of the warp and weft fibers. The Poisson's ratio for this analysis therefore focuses on the ratio in the low-strain region of operation, for axial strain less than one percent (Hursa et al., 2009). The Poisson ratios for orthotropic materials are verified using the ratio of elastic moduli provided in Equation 5.1.1 (Li and Barbič, 2014). The ratios shown in Equation 5.1.1 must be equal for Equation 1.4.7 to be symmetric. The Poisson's ratios estimated for the skin material are verified in Equations 5.1.2 and 5.1.3 respectively. Note that while the ratios are not exactly equal, they are sufficiently close within experimental error.

$$\frac{\nu_{12}}{E_{xx}} = \frac{\nu_{21}}{E_{yy}} \tag{5.1.1}$$

$$\frac{\nu_{12}}{E_{xx}} = \frac{0.297}{18.662} = 0.0159 \tag{5.1.2}$$

$$\frac{\nu_{21}}{E_{yy}} = \frac{0.727}{68.100} = 0.0107 \tag{5.1.3}$$

The values of Poisson's ratio ν_{12} and ν_{21} are therefore reasonable for the true values, although the difference in the ratios is significant. It is difficult to be precise in the calculation of Poisson's ratio, especially with the given response.

5.2 Neoprene

The following neoprene samples tested are of different durometer measurements. Unlike the other constituent components evaluated in this research, the actual coating used in the panel skin was not able to be tested individually. A commercially available neoprene is therefore evaluated as an equivalent substitute of the true coating material.

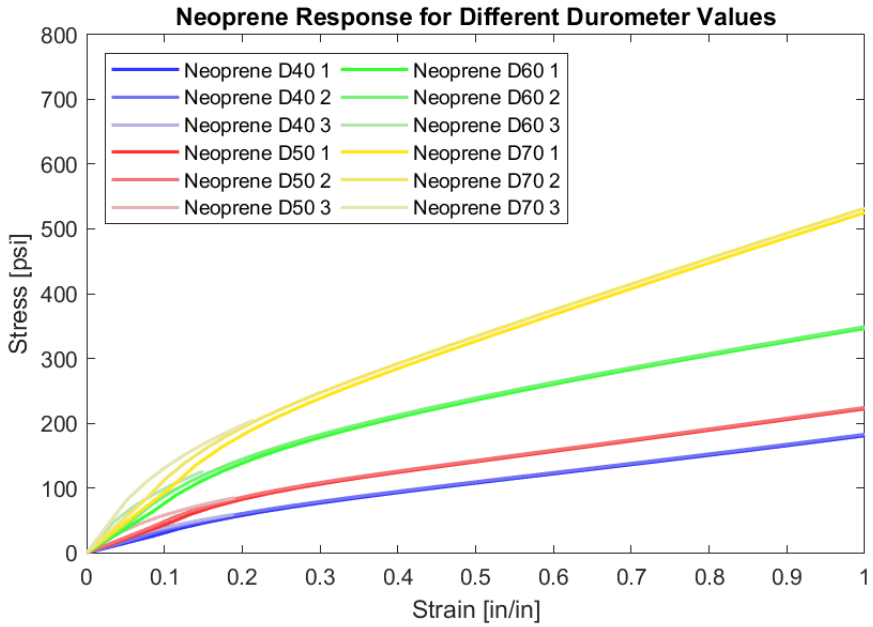

Figure 22. Stress-Strain Curves for Neoprene under Uniaxial Tension for Different Durometer levels

Table 3. Elastic Moduli for Neoprene

Durometer	E_1, ksi	E_2, ksi
40	0.3758	0.1862
50	0.5442	0.2081
60	0.9896	0.3204
70	1.1886	0.4665

Figure 22 demonstrates the stress-strain response of neoprene under uniaxial tension. Table 3 demonstrates the elastic modulus of the neoprene for each durometer value, denoted as E_1, and the slope of the stress-strain curve after 50% strain, denoted as E_2. It is evident from the relatively low elastic modulus of the neoprene relative to the modulus of the skin for all durometer values that the neoprene is not the dominating component of the skin material.

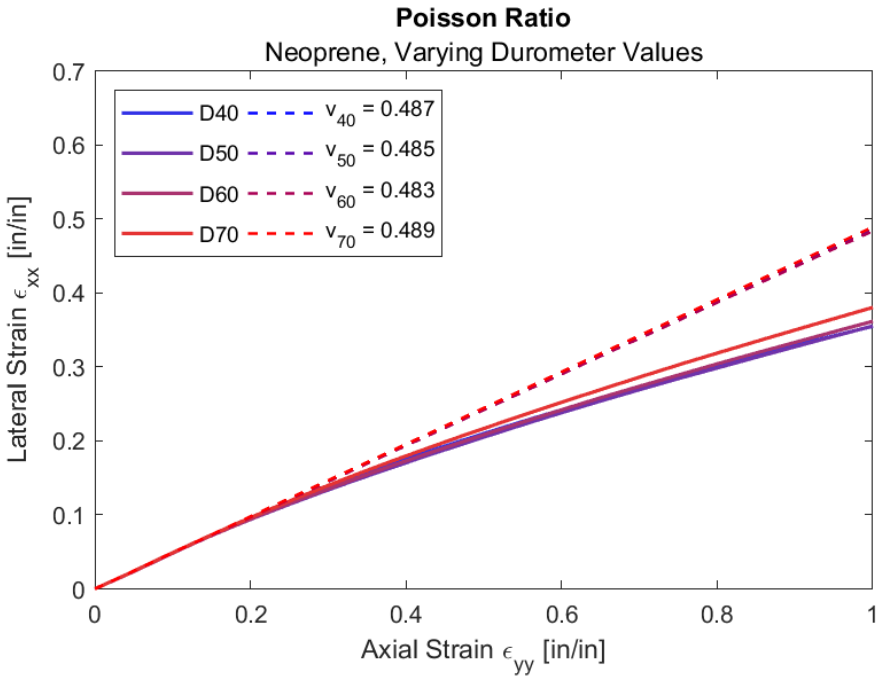

Figure 23. Poisson's Ratio for Neoprene for Different Durometer Levels

Figure 23 demonstrates the calculation of Poisson's ratio for the neoprene samples. Poisson's ratio is approximately 0.49 for all durometer values of neoprene. This result confirms the neoprene is at least quasi-incompressible, as is expected of a rubber material. Note that there is no directional dependence for the material properties of the neoprene since neoprene is expected to be isotropic.

5.3 Chafer Layer

The chafer layer alone was tested repeatedly in one session for the weft and the warp directions, respectively. Two separate samples of the chafer material were tested three times each.

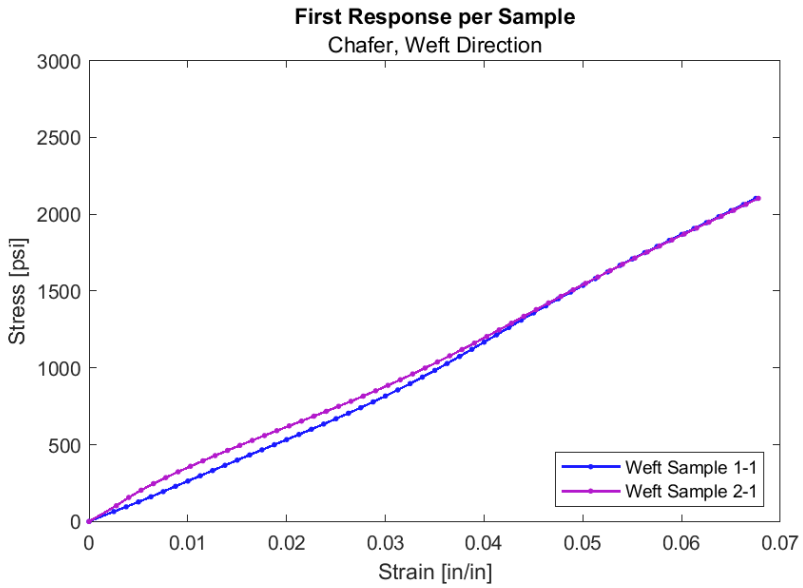

Figure 24. Stress-Strain Curve for Initial Loading of Chafer Sample in the Weft Direction, Per Sample

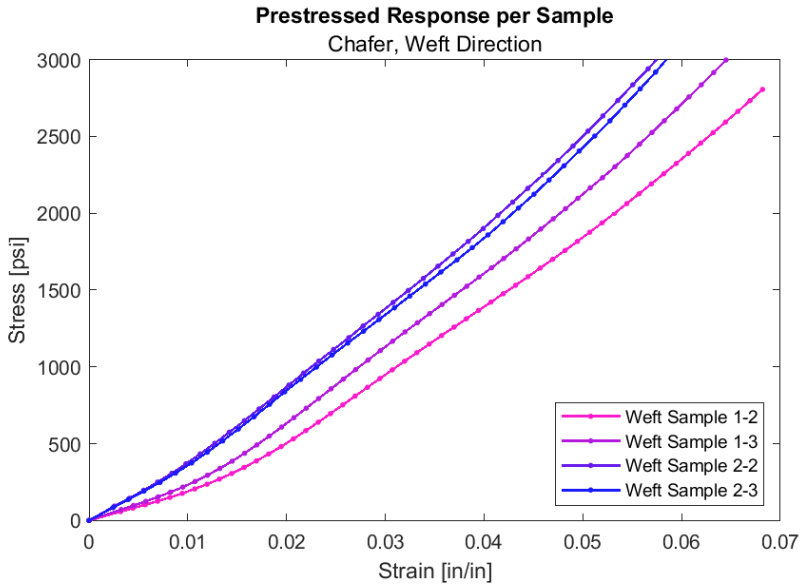

Figure 25. Stress-Strain Curve after Prestress for Chafer Sample in the Weft Direction

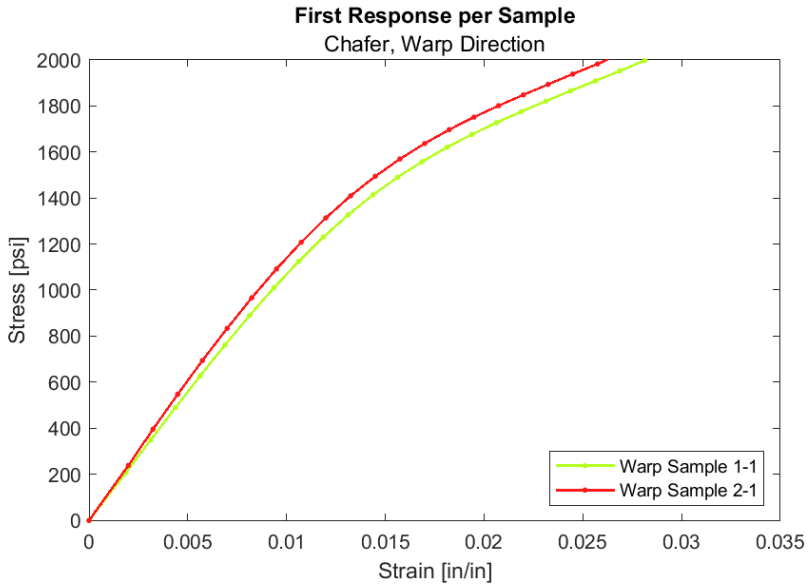

Figure 26. Stress-Strain Curve for Initial Loading of Chafer Sample in the Warp Direction, Per Sample

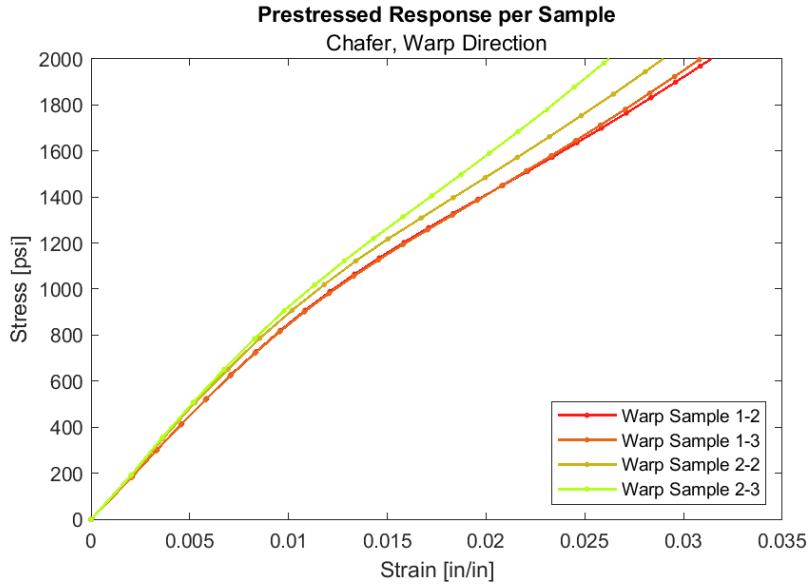

Figure 27. Stress-Strain Curve after Prestress for Chafer Sample in the Warp Direction

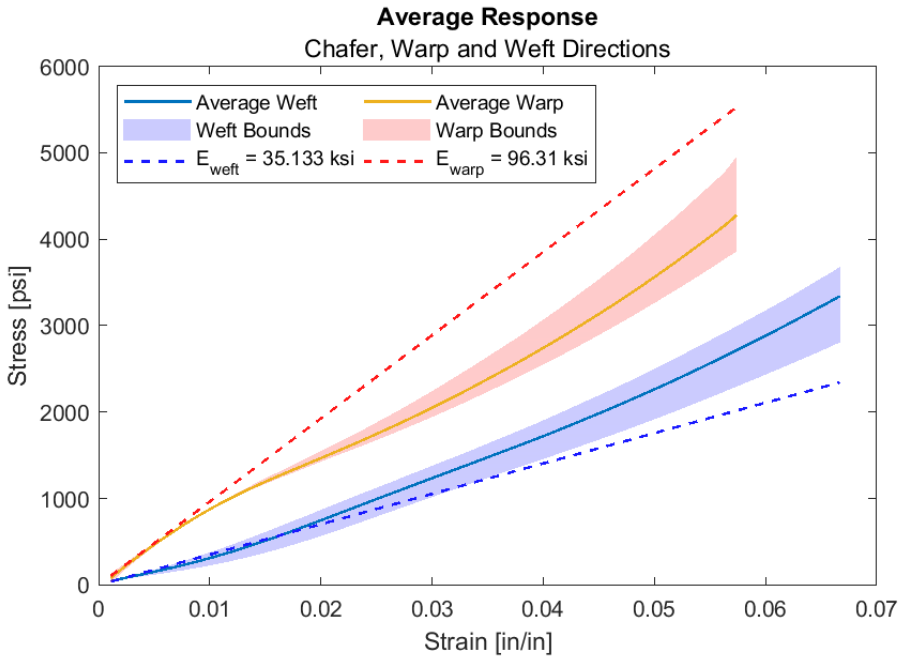

Figure 28. Average Stress-Strain Curve for Warp and Weft Directions for the Chafer Layer, with marked Elastic Moduli

Figures 24 and 25 show the uniaxial tension results for the same chafer material pulled in the weft direction. Similarly, Figures 26 and 27 show the uniaxial tension results for solely the chafer layer of the skin material pulled in the warp direction. The initial loading of each chafer sample are shown in Figures 24 and 26. Similar to the results for the skin material, the initial loading of the chafer samples yielded stress-strain responses significantly different in form than the prestressed responses. The previously proposed theory that the tightening and relaxing of the chafer layer caused such behavior in the skin material also would explain this behavior in the chafer layer alone.

Figure 28 shows the averaged, prestressed stress-strain response of the chafer layer and the effective elastic moduli for the warp and weft directions, respectively. The warp direction elastic modulus is approximately 31.417 ksi, while the weft direction elastic modulus is approximately 94.440 ksi. The larger elastic moduli in the chafer layer implies that the chafer layer has a larger contribution to the properties and response of the panel skin.

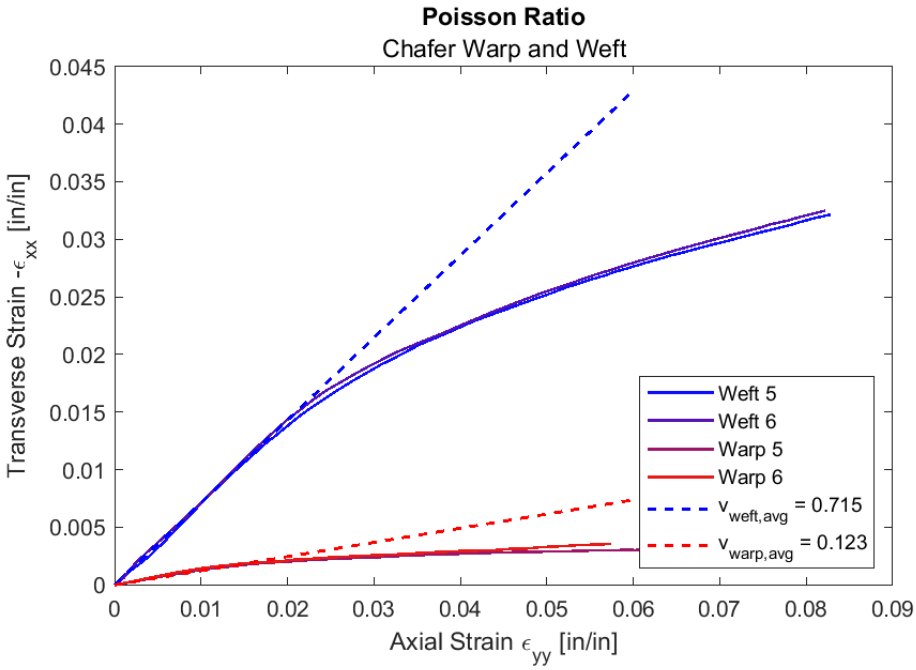

Figure 29. Poisson's Ratio for Warp and Weft Directions for the Chafer Layer

Figure 29 shows the estimation of Poisson's ratio for the chafer layer. Equations 5.3.1 and 5.3.2 demonstrate the verification of these values using Equation 5.1.1. Note that this relationship does not hold for the chafer layer as is expected.

$$\frac{\nu_{12}}{E_{xx}} = \frac{0.715}{35.133} = 0.0204 \tag{5.3.1}$$

$$\frac{\nu_{21}}{E_{yy}} = \frac{0.123}{96.308} = 0.0013 \tag{5.3.2}$$

5.4 Drop-Stitch Layer

The following data is for the drop-stitch fabric layer alone. Note that the data analyzed for the drop-stitch layer alone is taken from research conducted by teammate Milo Ferrazzoli (Ferrazzoli, 2019).

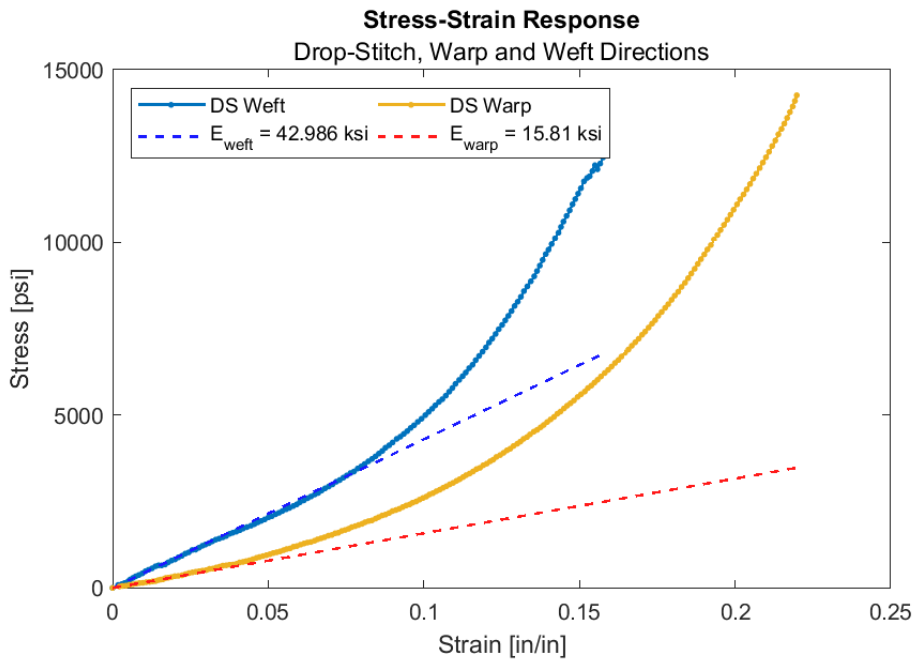

Figure 30. Stress-Strain Curve for Warp and Weft Directions for the Drop-Stitch Layer, with marked Elastic Moduli

Figure 30 shows the warp and weft response of the drop-stitch layer alone. Contrary to the skin response as a whole or the chafer layer response, the weft direction for the drop-stitch layer is stiffer than the warp direction. This result implies that the contribution of the drop-stitch layer to the tensile properties of the skin material is much smaller in the warp direction than in the weft direction.

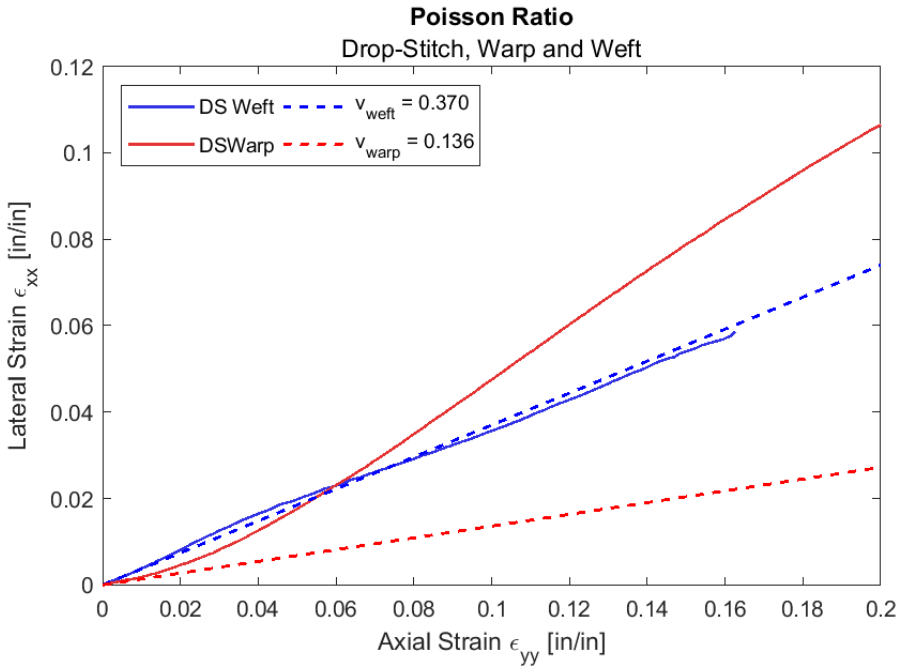

Figure 31. Calculation of Poisson's Ratio for Warp and Weft Directions for the Drop-Stitch Layer

The estimation of Poisson's ratio ν_{12} and ν_{21} for the orthotropic drop-stitch fabric layer are illustrated in Figure 31. Note again that for orthotropic materials, Equations 5.4.1 and 5.4.2 must each be equal (Li and Barbič, 2014). Note that in Figure 31 the Poisson ratio is only valid for axial strain less than approximately 2%.

$$\frac{\nu_{12}}{E_{xx}} = \frac{0.370}{42.986} = 0.0086 \tag{5.4.1}$$

$$\frac{\nu_{21}}{E_{yy}} = \frac{0.136}{15.812} = 0.0086 \tag{5.4.2}$$

5.5 Four-Point Panel Bend

A comparison between the Euler-Bernoulli beam assumption and experimental four-point bending may be executed using the equations derived in Chapter 3 and the estimated elastic modulus of 68.1 ksi for the warp direction of the skin material shown in Figure 20. The shear modulus G_{12} is taken from prior research to be 3.2

ksi (Taggart, 2018). Figures 32 through 39 show the results for panels inflated to 5, 10, 15, and 20 psi under four-point bending using the properties outlined in Chapter 4.

In Figures 32 through 35 the kinking parameter θ is taken to be zero. The total deflection is computed to be the sum of the bending deflection with $\theta = 0$ and the shear deflection. It can be seen that the predicted deflections are less than the experimentally observed deflections, especially at low inflation pressures. Introducing the empirical kinking parameter θ provides good agreement with experimental deflections, as shown in Figures 36 through 39.

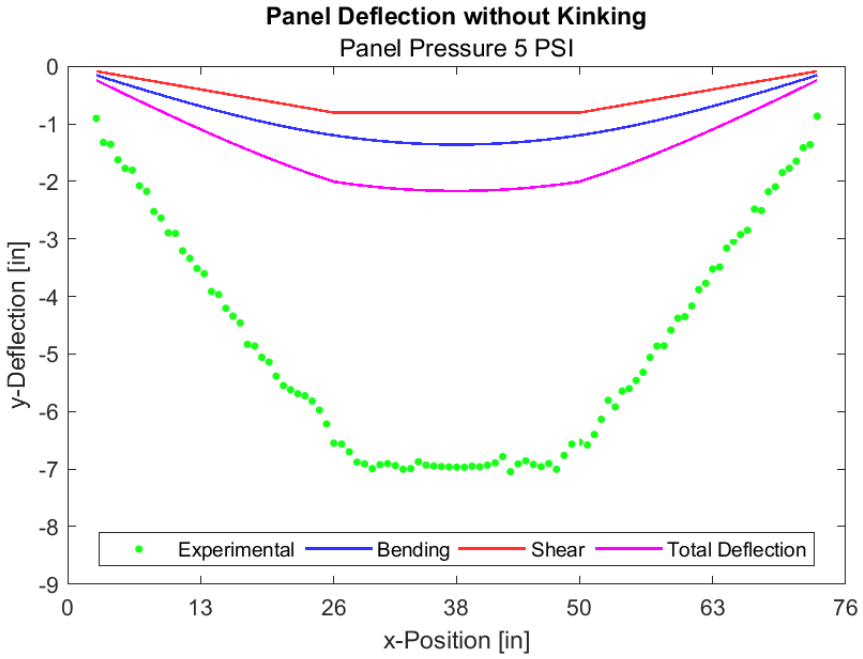

Figure 32. Comparison of classical beam bending, shear deformation, and the combined bending for 5 psi

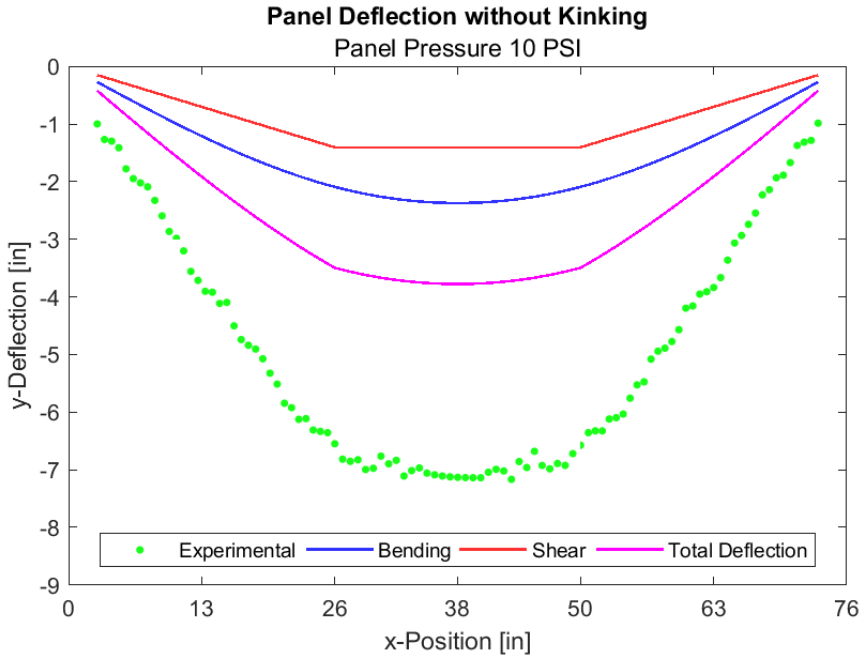

Figure 33. Comparison of classical beam bending, shear deformation, and the combined bending for 10 psi

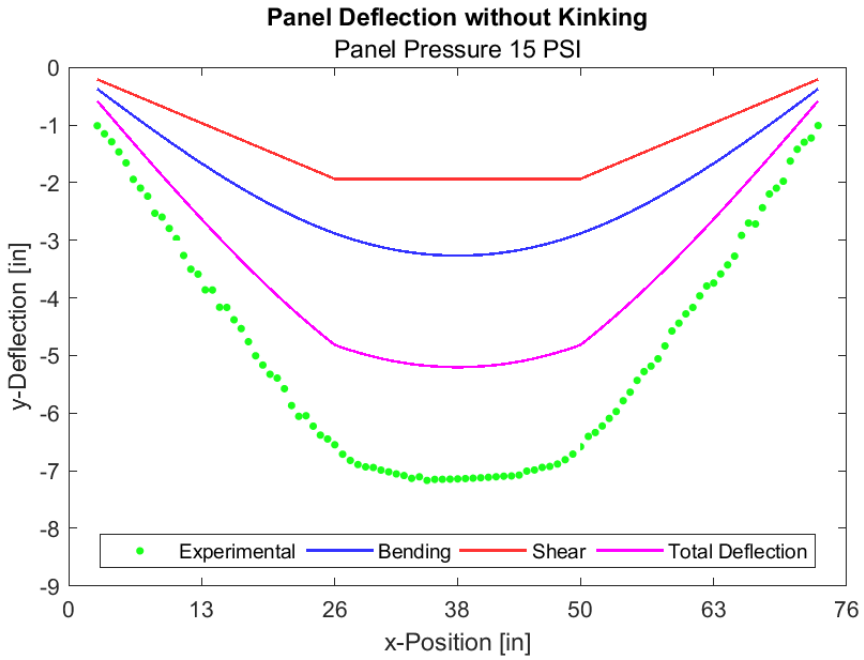

Figure 34. Comparison of classical beam bending, shear deformation, and the combined bending for 15 psi

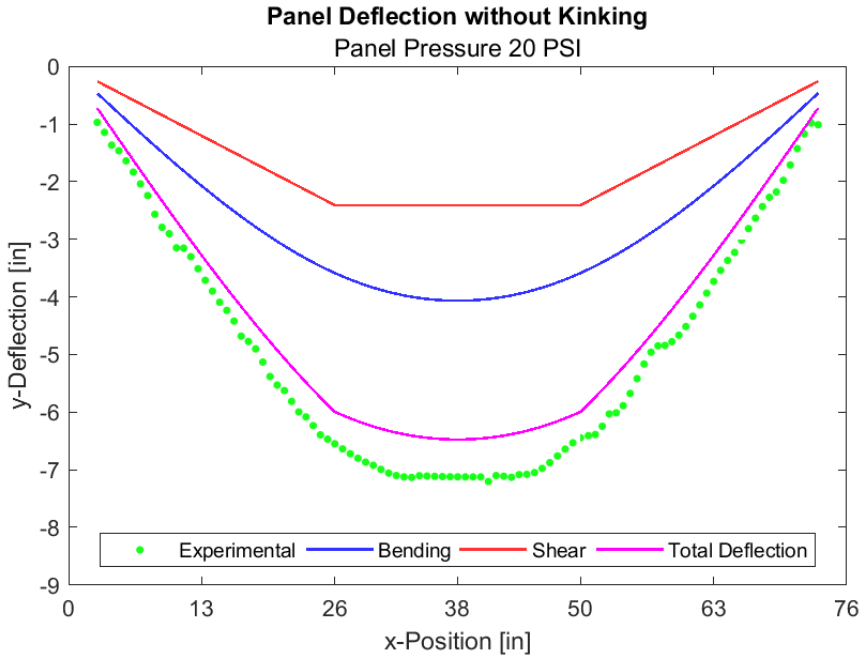

Figure 35. Comparison of classical beam bending, shear deformation, and the combined bending for 20 psi

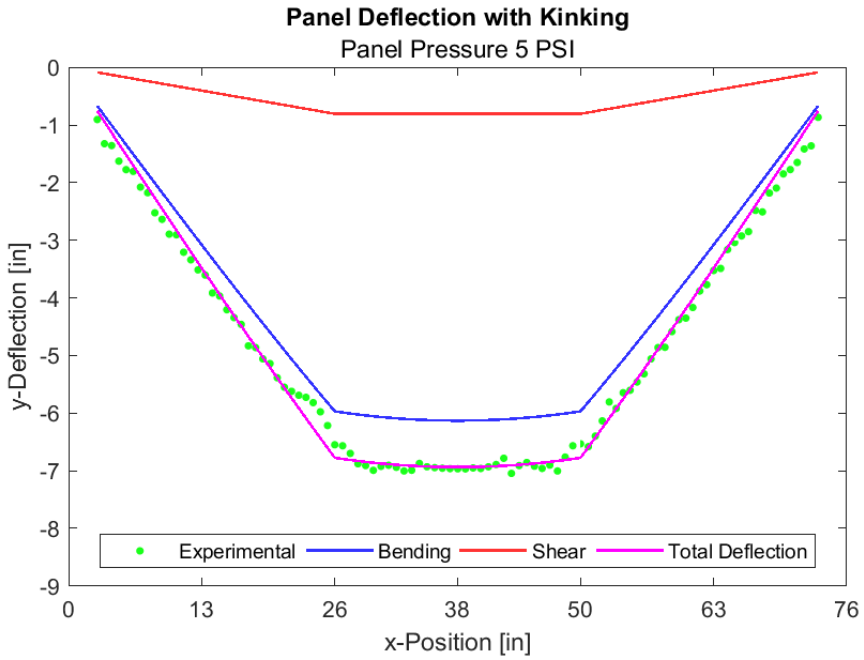

Figure 36. Comparison of modified beam bending with the term θ included, shear deformation, and the combined bending for 5 psi

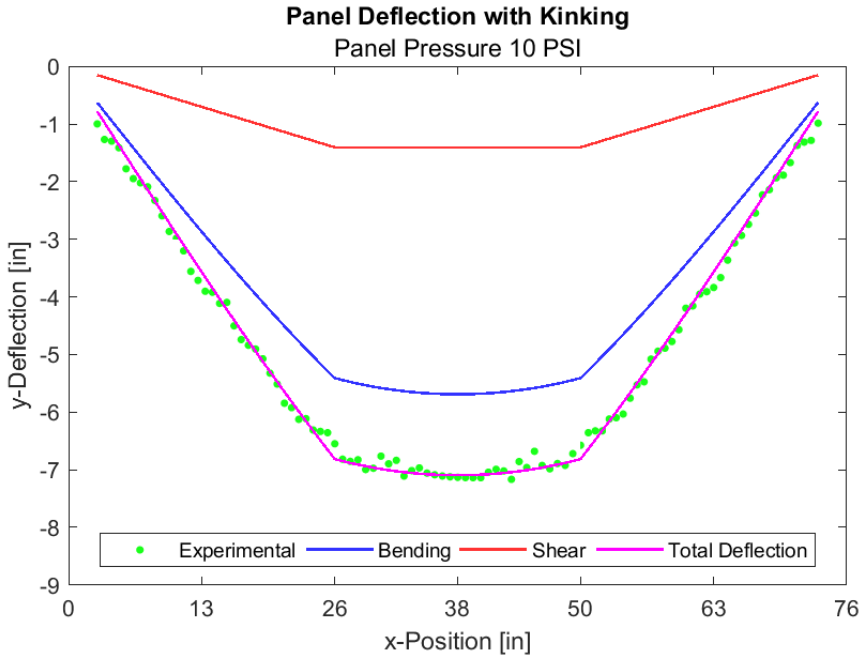

Figure 37. Comparison of modified beam bending with the term θ included, shear deformation, and the combined bending for 10 psi

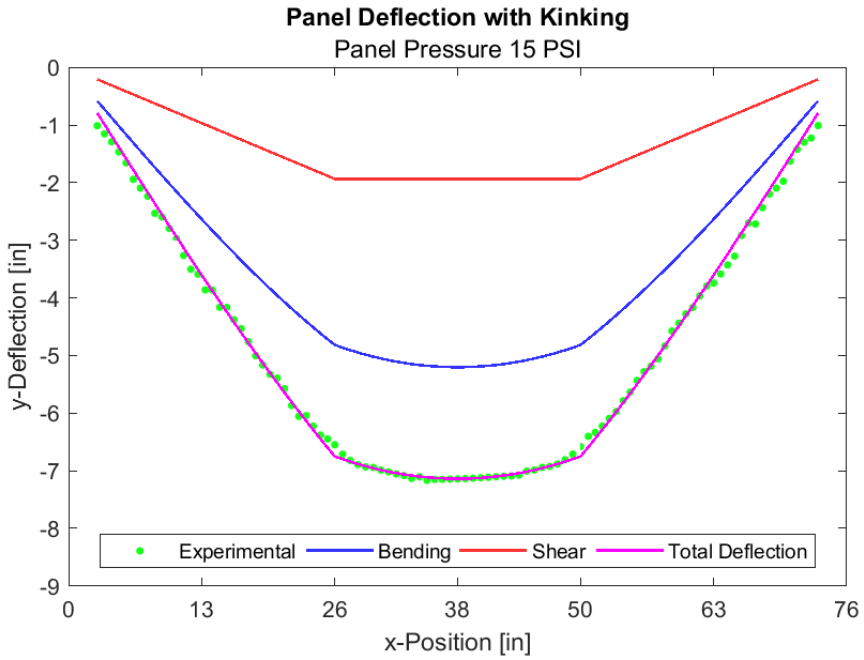

Figure 38. Comparison of modified beam bending with the term θ included, shear deformation, and the combined bending for 15 psi

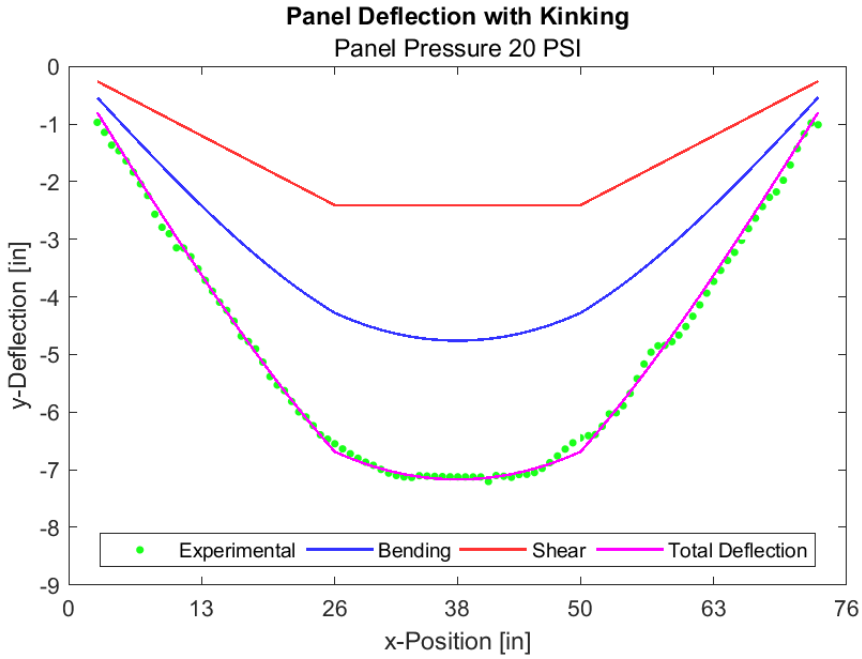

Figure 39. Comparison of modified beam bending with the term θ included, shear deformation, and the combined bending for 20 psi

Table 4. Average Percentage Difference between Beam-Theory and Experimental Results, No Discontinuity Term

PSI	**Bend**	**Shear**	**Combined**
5	81.24 ± 0.95	88.7 ± 0.88	69.95 ± 1.71
10	67.64 ± 1.50	80.52 ± 1.29	48.16 ± 2.50
15	55.52 ± 1.64	73.21 ± 1.75	28.73 ± 3.02
20	44.58 ± 1.87	66.63 ± 2.13	11.20 ± 3.53

The percentage difference between beam theory with no kinking, pure shear deformation, and the combined bending are tabulated in Table 4. The results demonstrate that there is significant error between the results estimated through beam theory equations and the experimental performance of these panels, therefore suggesting the need for the inclusion of an additional deformation mechanism.

Table 5. Estimates of θ and k_τ

PSI	$\theta(^\circ)$	$k_\tau(\frac{lb_f - in}{^\circ})$
5	10.51	174.28
10	7.31	436.63
15	4.26	1013.17
20	1.53	3588.53

Table 6. Average Difference between Beam-Theory and Experimental Results, Discontinuity Term Included

PSI	**Bend**	**Shear**	**Combined**
5	14.39 ± 5.97	88.7 ± 0.88	3.09 ± 6.85
10	21.63 ± 4.14	80.52 ± 1.29	2.14 ± 5.40
15	28.73 ± 3.02	73.21 ± 1.75	1.94 ± 4.66
20	34.99 ± 2.27	66.63 ± 2.13	1.61 ± 4.09

The derived beam theory equations which account for local deformation through the addition of θ may then be compared with the experimental results. The angle θ appears to be dependent upon inflation pressure, and therefore optimization of θ in order to best fit the experimental data was performed using the MATLAB script found in Appendix D.

The resulting value of θ and the effective torsional stiffness derived from θ for each inflation pressure are tabulated in Table 5. Note that the torsional stiffness k_τ increases exponentially with inflation pressure as $\theta \to 0$, indicating that the panel is intuitively increasing its rigidity with inflation pressure. The discontinuity variable θ decreases linearly with inflation pressure, with θ equaling zero at inflation pressure of approximately 22.33 psi.

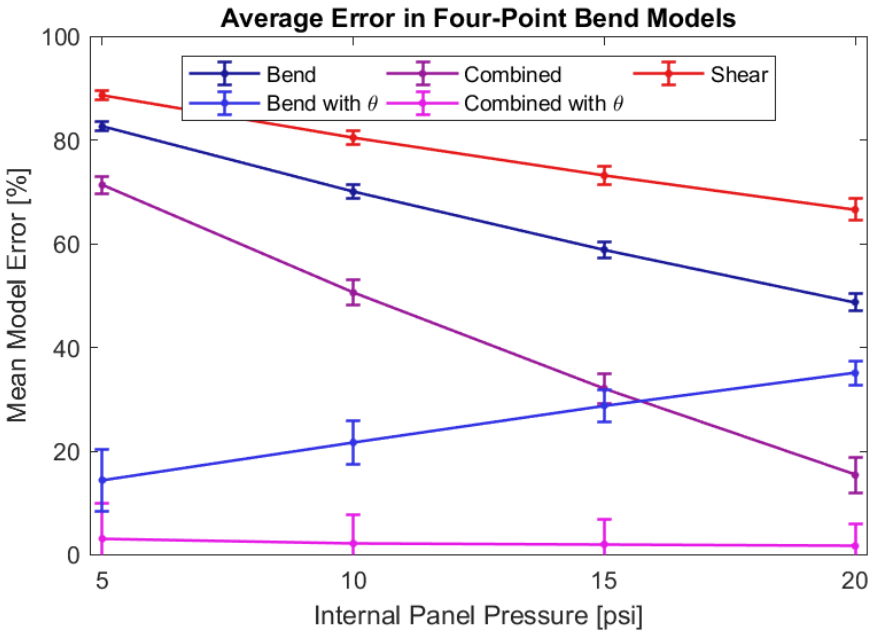

Figure 40. Average Error Comparison of Four-Point Panel Bending Models With and Without θ

Table 6 shows the percentage difference between the same four-point bending experimental results as used in Table 4 with the modified beam theory equations, the pure shear deformation, and the combination of both. A visual comparison between Tables 4 and 6 is provided in Figure 40. Note that the shear contribution is not dependent on θ, and therefore the error in the pure shear model does not change between 4 and 6.

It is evident from the data that the model including discontinuities at the load points and the deformation due to shear stresses is a significantly more accurate than the model from classical beam theory, therefore demonstrating that the drop-stitch inflatable structure may not be assumed to be an Euler-Bernoulli beam, especially at low inflation pressures. Table 5 demonstrates that as the inflation panel of the pressure increases, the discontinuity term θ tends toward zero. Therefore, for sufficiently high pressures, the model that includes the discontinuity becomes equivalent to the traditional Euler-Bernoulli beam theory, and then the combined classical and shear deflection are sufficient in order to model the beam. Figure 40 also illustrates how the classical and discontinuous beam models converge toward each other with an increase in internal panel pressure.

CHAPTER 6

Conclusions

6.1 Uniaxial Tensile Test

The results of the uniaxial tension test are successful in generating stress-strain responses for the drop-stitch inflatable woven panel skin material and the constituent materials which comprise said skin material. The overall data demonstrated that within a low-strain region of less than one percent strain, the response of the skin material and its components are all approximately linear. Further still, the skin material as a whole and the neoprene show approximately linear behavior for strains less than approximately three percent.

The skin material, the chafer layer, and the drop-stitch layer are all shown to be orthotropic through the differences in the weft and warp direction properties and characteristics. The chafer layer of the skin material is shown to be the dominating component of the skin material, having the stiffest response and largest elastic modulus of the components.

Inconsistencies were found in the measurement of Poisson's ratio for the skin material and its constituent components, particularly in the chafer layer of the skin. The errors and unusual nature of the Poisson's ratio may be attributed to nonlinear or anisotropic qualities of the materials due to the nature of the woven fabric. Further research into the Poisson ratio of the woven fabrics may be required.

The use of digital image correlation is demonstrated as a viable method for non-invasive displacement and strain field measurement. One example of this verification is the accurate measurement of Poisson's ratio for the neoprene. The neoprene samples were shown as nearly incompressible, as is expected for rubber materials.

6.2 Model Comparisons

The comparison of the four-point bending models demonstrated the inaccuracy of the assumption that the drop-stitch inflatable woven panel is able to be treated as an Euler-Bernoulli beam. The pure bending result for each inflation pressure is significantly inaccurate for low inflation pressures. The model is improved through the addition of deflection due to shear strains, and then further improved by the inclusion of a kinking parameter θ. Although θ is a best-fit variable designed to minimize error, the fact that a nonzero θ improves the model so significantly illustrates the importance of accounting for the local deformation and skin buckling near the load-point in future models. This conclusion is further supported by the fact that as the panel pressure increases, the local deformation at the load-points loses its effect and $\theta \to 0$.

6.3 Future Research

It is apparent that the modeling of these drop-stitch inflatable woven structures and the characterization of the skin material properties is complex and difficult to characterize accurately. The woven fabric composite skin material is difficult to fully characterize by itself, without the added complication of modeling the inflatable structure. Future research into the characterization of the panel skin material and its constituent components through additional uniaxial and biaxial testing is recommended. The properties gathered from these additional tests could be used in order to either linearize the skin properties within the range of operation or could be used in order to generate robust nonlinear material parameters in finite element simulations. The skin could also be analyzed using composite-laminate approaches in order to better characterize its behavior.

Further research into the individual components of the skin material and how these components interact under loading within the skin are also important areas of research to consider. Further understanding of the material properties of the skin material and its constituent components is required in order to understand their behavior under loading, especially in order to account for the abnormalities found in Poisson's ratio for said materials.

The evaluation of other panel configurations and panel skin materials is also an important research topic to consider, especially to verify and generalize the panel and skin modeling. Finite element models of the panel as a whole and the local contact region would also be valuable in order to observe the complicated deformation mechanisms and discontinuities at the load points.

Three-dimensional digital image correlation could be used in order to more accurately capture the strains in the panel skin under panel loading in order to accurately determine the range of operation for the skin. The out-of-plane panel deformation of uniaxial or biaxial samples, which had been assumed to be negligible for this research, could similarly be captured and analyzed using three-dimensional digital image correlation.

LIST OF REFERENCES

Aboshio, A., Green, S., and Ye, J. (2015). Experimental investigation of the mechanical properties of neoprene coated nylon woven reinforced composites. *Composite Structures*, 120:386–393.

Barnfield, L. (2016). Inflatable hangars and structures. Accessed on 4-05-2019.

Blaber, J., Adair, B., and Antoniou, A. (2015). Ncorr: Open-source 2d digital image correlation matlab software. *Experimental Mechanics*.

Budynas, R. G. and Nisbett, J. K. (2011). *Shigley's Mechanical Engineering Design*, chapter 4, pages 87–92,162–169. McGraw-Hill, New York, NY, 9 edition.

Cavallaro, P. V., Hart, C. J., and Sadegh, A. M. (2013). Mechanics of air-inflated drop-stitch fabric panels subject to bending loads. In *ASME International Mechanical Engineering Congress and Exposition*, San Diego, CA.

Cavallaro, P. V., Sadegh, A. M., and Quigley, C. J. (2007). Decrimping behavior of uncoated plain-woven fabrics subjected to combined biaxial tension and shear stresses. *Textile Research Journal*, 77(6):403–416.

Collins, J., Rusby, H. R., and Staab, G. H. (2010). *Mechanical Design of Machine Elements and Machines: A Failure Prevention Perspective*, chapter 4, pages 123–137. Wiley, Hoboken, NJ, 2 edition.

Comer, R. and Levy, S. (1963). Deflections of an inflated circular cylindrical cantilever beam. *American Institute of Aeronautics and Astronautics (AIAA) Journal*, 1(7):1652–1655.

DiGiovanna, L. (2013). Characterizing the mechanical properties of drop stitch inflatable structures. Bachelor's thesis.

Falls, J. and Waters, J. (2011). Bending tests of inflatable dropstitch panels. In *11th International Conference on Fast Sea Transportation, FAST*.

Felicissimo, R. (2015). Exploration of the mechanical properties of both ridged and inflated drop stitch fabric material. Master's thesis, City University of New York.

Ferrazzoli, M. (2018-2019). data set, personal correspondence.

Graczykowski, C. and Heinonen, J. (2006). Adaptive inflatable structures for protecting wind turbines against ship collisions. Technical Report VVT Working Papers 59, IPPT - Institute of Fundamental Technology Research (Poland).

Halswell, P., Wilson, P., and Taunton, D. (2012). Hydroelastic inflatable boats: Relevant literature and new design considerations. *International Journal of Small Craft Technology*, 154 (B1).

Harilal, R. and Ramji, M. (2014). Adaptation of open source 2d dic software ncorr for solid mechanics applications. Technical report, Indian Institute of Technology.

Ho, Q. D. (2015). An assessment of the accuracy of the euler-bernoulli beam theory for calculating strain and deflection in composite sandwich beams. Master's thesis, University of New Orleans.

Hodge, J. (2018). Sea eagle 472rl razorlite inflatable drop stitch kayak. Accessed on 4-05-2019.

Hulton, A. W., Cavallaro, P. V., and Hart, C. J. (2017). Modal analyis and experimental testing of air-inflated dropstitch fabric structures used in marine applications. In *Proceedings of 2017 International Mechanical Engineering Congress and Exposition*.

Hursa, A., Rolich, T., and Ražić, S. E. (2009). Determining pseudo poisson's ratio of woven fabric with a digital image correlation method. *Textile Research Journal*, 79(17):1588–1598.

Justusson, B. P., Spagnuolo, D. M., and Yu, J. H. (2013). Assessing the applicability of digital image correlation (dic) technique in tensile testing of fabric composites. Technical report, Army Research Laboratory.

Kelly, P. (2015). Engineering solid mechanics. Accessed on 3-21-2019.

Li, Y. and Barbič, J. (2014). Stable orthotropic materials. In *Proceedings of the ACM SIGGRAPH/Eurographics Symposium on Computer Animation*, SCA '14, pages 41–46, Aire-la-Ville, Switzerland, Switzerland. Eurographics Association.

Main, J., Peterson, S., and Strauss, A. (1994). Load-deflection behavior of space-based inflatable fabric beams. *Journal of Aerospace Engineering*, 7(2):225–238.

Majumdar, A. (2014). Fabric manufacturing - i. Accessed on 4-05-2019.

Roylance, D. (2008). Mechanical properties of materials. Accessed on 3-21-2019.

Roylance, D. (2010). Laminate composite plates. Accessed on 3-21-2019.

Sadegh, A. M. and Cavallaro, P. V. (2006). Air-inflated fabric structures. In *Mark's Standard Handbook for Mechanical Engineers*, pages 20.108–20.118. McGraw-Hill, 11 edition.

Sadegh, A. M. and Cavallaro, P. V. (2012). Mechanics of energy absorbability in plain-woven fabrics. *Journal of Engineered Fibers and Fabrics*, 62:495–509.

Taggart, D. G. (2018). Simulation models for drop stitch inflatable panels. unpublished, presentation.

Van, A. L. and Wielgosz, C. (2005). Bending and buckling of inflatable beams: Some theoretical results. *Thin-Walled Structures*, 43(8):1166–1187.

APPENDIX A

Image Reformatting MATLAB Function

```
function rect = batchcrop(folder,ext,rotang,newname,oldname,num,rect)
    % batchcrop.m
    % Michael Smith --- Last Edit: 7/24/2018
    % Crops and renames multiple images with increasing integer name
    % scheme
    % INPUT -----
    %       folder  -   Location of images
    %       ext     -   File extension (Default: .JPG)
    %       rotang  -   Angle of Rotation for Image (deg, CCW)
    %       newname -   New naming base for modified images
    %       oldname -   "Base" name of image batch
    %                   Default: '', i.e. use all images in folder
    %       num     -   Use every nth frame
    %                   Default: num = 1, use every frame
    %       rect    -   Crop Settings, in format:   [x0 y0 dx dy]
    % OUTPUT ----- saved to destination folder (Images)

    %% Input Checks
    if nargin < 1, folder = '..\.';     end     % DEF: Folder up
    if nargin < 2, ext = '.JPG';        end     % DEF: .JPG ext
    if nargin < 3, rotang = 0;          end     % DEF: 0 deg rot.
    if nargin < 4, newname = 'image';   end     % DEF: 'image_0'
    if nargin < 5, oldname = '';        end     % DEF: Unspec.
    if nargin < 6, num = 1;             end     % DEF: Step size 1

    if ~isscalar(num), num = 1;         end     % Nonscalar --> 1

    %% Initialization
    % Save current folder, go to image folder
    oldfolder   = cd(folder);
    files       = dir(['**\*' ext]);
    oldnames    = {files.name};
    if oldname, oldnames = oldnames(contains(oldnames, oldname)); end

    % Set Crop Dimensions
    if nargin < 7
        I        = imread(oldnames{1});
        [~,rect] = imcrop(I);
    end

    %% Image Looping
    indvec = 1:num:length(oldnames);
    for p = 1:length(indvec)
        n = indvec(p);
        %Image Processing
        I      = imread(oldnames{n});  % Read current image
        I1     = imcrop(I, rect);      % Crop current image
        I1     = imrotate(I1, rotang); % Rot. current image

        % Save modified image
        imwrite(I1, [newname '_' num2str(p-1) ext])
    end

    %% Finalization
    cd(oldfolder)               % Return to previous folder
    str = 'Complete Status:\t%s --> %s\tTotal: %d\tFormatted: %d\n';
    fprintf(str, oldname, newname, length(oldnames), length(indvec))
end
```

APPENDIX B

Ncorr2D Post-Processing MATLAB Function

```
function M = ncorr_post(fnames, Fdat, dim, modz, dt, folder)
    % ncorr_post.m
    % Michael Smith --- Last Edit: 01/23/2018
    % Generates Stress-Strain Data from Ncorr2D and U/BTM Data
    % INPUT -----
    %       filenames:  Names of files to be analyzed (assumed .mat)
    %       Fdat:       Matrix file of measured Force-Time Data
    %                   >> Data is stored under
    %                       "Time", "Force", "Displacement" headers
    %       dims:       Dimension of the sample cross-section
    %                   >> [dx dy dz]
    %       modz:       Cell array of cat; Primary sort cat
    %       dt:         Time step between frames
    %       folder:     Folder containing data mat files
    % OUTPUT ----
    %       M:          Structure containing Stress-Strain data
    %       >>  M.(name).force:    Force data                (F)
    %       >>  M.(name).dz:       Crosshead Displacement    (dz)
    %       >>  M.(name).stress:   Stress data, Estimated    (sigma)
    %       >>  M.(name).exx:      Strain data, Transverse   (exx)
    %       >>  M.(name).eyy:      Strain data, Axial        (eyy)
    %       >>  M.(name).exy:      Strain data, Shear        (exy)
    %       >>  M.(name).time;     Equilized Time            (t)
    %       >>  M.(name).v:        Poisson's Ratio (-exx/eyy)
    % [Additional Outputs added for verification]
    %% Input Checks
    if nargin < 2, error('Not enough input arguments'), end
    if nargin < 3, modz     = {''};                     end
    if nargin < 4, dim      = [1 1 1];                  end
    if nargin < 5, dt       = 2*ones(size(fnames));  end
    if nargin > 5, addpath(folder);                     end

    %% Main Function
    disp('START ---')
    % Generating Data
    for n = 1:length(fnames)
        %% Data Loading and Formatting
        tic
        fprintf('%s', fnames{n})
        if length(dt) == 1, dt = dt*ones(length(fnames),1); end

        if ~contains(fnames{n}, modz), continue
        else, dtm = dt(n);
        end

        % Load data and adjust vector sizes
        load([fnames{n} '.mat'], 'data_dic_save')
        avgdat      = ncorr_postprocess(data_dic_save,dtm);

        % >> Load Force and Interpolate to same time scale as frames
        time        = Fdat.(fnames{n}).Time;
        if      max(contains(fieldnames(Fdat.(fnames{n})), ...
                'Force'))
            force   = Fdat.(fnames{n}).Force;
        else
            force   = Fdat.(fnames{n}).Load;
```

```
end
force       = interp1(time, force, avgdat(:,1), 'linear');

% >> Load Disp. and Interp1 to same time scale as frames
if      max(contains(fieldnames(Fdat.(fnames{n})), ...
        'Displacement'))
    dz      = Fdat.(fnames{n}).Displacement;
elseif  max(contains(fieldnames(Fdat.(fnames{n})), ...
        'Stroke'))
    dz      = Fdat.(fnames{n}).Stroke;
else
    dz      = Fdat.(fnames{n}).Extension;
end
dz          = interp1(Fdat.(fnames{n}).Time, dz, ...
                avgdat(:,1), 'linear');

%% Strain Handling
% >> Define Strain
strain{1}   = avgdat(:,2);  % exx
strain{2}   = avgdat(:,3);  % eyy
strain{3}   = avgdat(:,4);  % exy

% >> Define Displacements
delta{1}    = avgdat(:,5);  % U Displacement
delta{2}    = avgdat(:,6);  % V Displacement

% >> Extract Span of Interest
imax        = find(force == max(force));
ind         = find((force <= max(force)) ...
            & (force >= min(force(force>0))));
ind         = ind(ind <= imax);

force       = force(ind);
dz          = dz(ind);
for b = 1:3
    temp        = strain{b};
    strain{b}   = temp(ind);
end
for b = 1:2
    temp        = delta{b};
    delta{b}    = temp(ind);
end, clear temp b

%% Stress Calculation

if contains(fieldnames(Fdat),'dir')
    % >> If direction of loading is specified
    pind    = flip(nchoosek(1:3,2));
    across  = (Fdat.dir).*pind;
    across  = dim(across(1))*dim(across(2));  % Ac = W*h
else
    % >> Else assume Loading is in y-direction
    across  = (dim(1)*(1 + strain{1})).*dim(3);
end
stress  = force./across;

%% Poisson's Ratio
v           = -avgdat(:,2)./avgdat(:,3);
% Axial > x, Lateral > y

%% Data Storage
M.(fnames{n}).force      = force;
M.(fnames{n}).stress     = stress;
M.(fnames{n}).dz         = dz;
M.(fnames{n}).exx        = strain{1};
M.(fnames{n}).eyy        = strain{2};
M.(fnames{n}).exy        = strain{3};
```

```
        M.(fnames{n}).udisp      = delta{1};
        M.(fnames{n}).vdisp      = delta{2};
        M.(fnames{n}).time       = time(ind);
        M.(fnames{n}).v          = v(ind);

        fprintf(',%s %0.2f\t Time: %g\n', ...
            repmat(' ', [20-length(fnames{n}) 1]), dtm, toc)
    end

    %% Finalization
    if nargin > 5, rmpath(folder); end
    disp('END ---')
end

%% Subfunctions
function avgdat = ncorr_postprocess(data_dic_save,dt)
    % ncorr_postprocess.m
    % Michael Smith --- Last Edit: 7/18/2018
    % Transforms Ncorr2D output data into
    %   mean strain values per image
    % INPUT -----
    %       data_dic_save  -   Output structure from Ncorr
    %       dt             -   Sampling rate for images (sec)
    % OUTPUT ----
    %       avgdat         -   Vector of:
    %           [{time} {med. exx} {med. eyy} {med. exy}]

    %% Main Function
    strains     = data_dic_save.strains;
    delta       = data_dic_save.displacements;
    avgdat      = zeros(length(strains),6);
    avgdat(:,1) = dt*(1:length(strains))';
    types       = {'plot_exx_ref_formatted', ...
                   'plot_eyy_ref_formatted', ...
                   'plot_exy_ref_formatted', ...
                   'plot_u_dic', ...
                   'plot_v_dic'};
    for t = 1:3   % Type of Strain (exx,eyy,exy)
        for n = 1:length(strains)
            eps             = strains(n).(types{t});
            eps( ~any(eps,2), : ) = [];     % Remove zero rows
            eps( :, ~any(eps,1) ) = [];     % Remove zero columns
            avgdat(n,t+1)   = median(median(eps));  % Current: median
            % >> Goal: Better averaging statistic
        end
    end

    for t = 4:5
        for n = 1:length(delta)
            dxy             = delta(n).(types{t});
            dxy( ~any(dxy,2), : ) = [];     % Remove zero rows
            dxy( :, ~any(dxy,1) ) = [];     % Remove zero columns
            avgdat(n,t+1)   = median(median(dxy));  % Current: median
        end
    end
end
```

APPENDIX C

Four-Point Bend Tracking MATLAB Script

```
function [x,y] = imbeam(imname,dxdu,dydv,method,uniy,per,imname_orig)
    % imbeam.m
    % Michael Smith --- Last Edit: 6/10/2018
    % Extract seam line in 4-point bending test of Inflatable Struct
    % INPUTS:       imname  - Name of the image to be analyzed
    %                 dxdu  - x Scale Factor (pixel to x)
    %                 dydv  - y Scale Factor (pixel to y)
    %               method  - Unique Point Filtering Method
    %                 uniy  - Logic Check, make y unique
    %                  per  - Logic Check, bwperim binarization
    %               mirror  - 'Mirror' Data for Symmetric Loads
    %          imname_orig  - Name of undoctored image for display
    % OUTPUTS:           x  - x coordinates of curve
    %                    y  - y coordinates of curve
    %% Conditional Operation
    if nargin < 7,  imname_orig = imname; end
    if nargin < 6,  per = 0; end
    if nargin < 5,  uniy = 0; end

    %% Initial Image Processing
    I   = imread(imname);                   % Load Image for Analysis
    I0  = imread(imname_orig);              % Load Image for Display
    BW = imbinarize(rgb2gray(I),.2);        % Binarize Image (Alpha)
    if per
        BW = bwperim(BW);                   % Isolate Perimeters
    end
    bound = bwboundaries(BW);               % Boundary Coordinates
                                            % (Cell format)
    N     = [];
    for k = 2:length(bound)                 % First Cell: Image Box
       b = bound{k};                        % Other Cell: Small Seg
       if length(b) > 15                    % Length of Viable Seg
           n = length(b);
           N(end+(1:n),:) = b;              % Collect Viable Seg
       end
    end

    if ~uniy
        [Nx, ~, subs] = unique(N(:,2));     % Isolate unique x
        Ny = accumarray(subs, N(:,1), ...   % Isolate matched y
             [], method);
        x = (Nx - min(Nx))*dxdu;            % Scale x coordinates
        y = (min(Ny) - Ny)*dydv;            % Scale y coordinates
    else
        x = (N(:,2) - min(N(:,2)))*dxdu;    % Scale x coord. (NU)
        y = (min(N(:,1)) - N(:,1))*dydv;    % Scale y coord. (NU)
    end
    % Alternate Functions: @max, @min, @median, @mean, @custom_fn

    if nargout == 0
        figure, imshow(I0), hold on, plot(Nx,Ny,'.','Markersize',11)
    end
end
```

APPENDIX D

Inflatable Panel Model MATLAB Script

```
% Dr. David Taggart, Michael Smith
% 15 March 2019
% beam_deflection.m
% Modeling of DS Inflatable Panel Deflection

clear variables, close all
load bend_data
b   = 20;               % Width of Rectangular Panel Section    (in)
h   = 0.055;            % Thickness of Panel Skin               (in)
r   = 2;                % Radius of Panel Sidewall              (in)
d   = 2;                % Rectangular Section to Origin         (in)
E   = 68.10e3;          % Elastic Modulus of Skin (Warp)        (psi)
G   = 3200;             % Shear Modulus of Skin                 (psi)
pressure    = [5 10 15 20];
Pmax        = [140.9; 245.6; 338.3; 421.1];
L   = 76;               % Span between Supports                 (in)
a   = 26;               % Length to Load                        (in)

%% Area Moment of Inertia
Ix_semi = (pi/8)*((r+2*h)^4-r^4); % w + h = n*h + h = 2h
Ix_rect = b*h^3/12+b*h*(d+h/2)^2;
I       = 2*Ix_rect + 2*Ix_semi;

%% Cross-Sectional Areas
Asw     = pi*((r+2*h)^2-r^2);       % Area of the Shear Walls
Ars     = 2*b*h;                    % Area of Rect. Sections
Atot    = Asw + Ars;                % Total Area

%% Main Function
x_exp = x;
S = cell(2*length(pressure),1);
for ip=1:2*length(pressure)
    if ip > length(pressure)
        slopechk = 1;
        v_exp   = ydat(:,ip-length(pressure));
        P       = Pmax(ip-length(pressure));
        S{ip}.press = pressure(ip-length(pressure));
        S{ip}.type  = 'Modified';
    else
        slopechk = 0;
        v_exp   = ydat(:,ip);
        P       = Pmax(ip);
        S{ip}.press = pressure(ip);
        S{ip}.type  = 'Classical';
    end

    S{ip}.v_exp = v_exp;
    S{ip}.x_exp = x_exp;
    S{ip}.P     = P;
    S{ip}.E     = E;
    S{ip}.G     = G;
    S{ip}.I     = I;
    S{ip}.a     = a;
    S{ip}.L     = L;
    S{ip}.Area  = Asw;
```

```
    if ip == 4
        v_bending_fea   = -6.354;
        v_total_fea     = -6.808;
        v_shear_fea     = v_total_fea-v_bending_fea;
        v_total_fea     = -6.808;
    end
    disp([' --- Pressure = ' num2str(S{ip}.press) ' ---'])
    if slopechk == 1
        theta           = fminsearch(@(theta) ...
                          deflection_error(theta,S{ip}),0);
        theta_degree    = theta*(180/pi);
        S{ip}.k_torsion = (P*a/2)/theta_degree;
    else
        theta           = 0;
        theta_degree    = theta*(180/pi);
    end

    [v,   vb,   vs   ]  = deflection(x_exp, theta, S{ip});
    [v_ms,vb_ms,vs_ms]  = deflection(L/2,   theta, S{ip});
    strain_bend         = (P*a/2)*d/(E*I);
    shearstr_sw         = atan((2*(P/2)*a/(Asw*G))/a);
    shear_rot           = atand((2*(P/2)*a/(Asw*G))/a);
    k_b                 = abs(P/vb_ms);          % Bend
    k_bs                = abs(P/v_ms);           % Bend + Shear
    k_exp               = abs(P/v_exp(50));      % Experimental

    S{ip}.strain_bend   = strain_bend;
    S{ip}.shear_strain  = shearstr_sw;
    S{ip}.shear_rot     = shear_rot;
    S{ip}.v             = v;
    S{ip}.vb            = vb;
    S{ip}.vs            = vs;
    S{ip}.verr          = (v_exp - v )./v_exp * 100;
    S{ip}.vberr         = (v_exp - vb)./v_exp * 100;
    S{ip}.vserr         = (v_exp - vs)./v_exp * 100;
    S{ip}.k_b           = k_b;
    S{ip}.k_bs          = k_bs;
    S{ip}.k_exp         = k_exp;
    S{ip}.theta         = theta;
    S{ip}.thetad        = theta_degree;
end

save('BeamDat.mat','S')
%% Subfunctions
function err_tot = deflection_error(theta,S)
    % Compute difference between experimental data
    % and analytical models
    x_exp   = S.x_exp;
    v_exp   = S.v_exp;
    v       = deflection(x_exp,theta,S);
    if size(v) ~= size(v_exp), v_exp = v_exp'; end
    err_tot = sqrt(mean((v-v_exp).^2));
end

function [v,vb,vs]=deflection(x,theta,S)
    P = S.P;    E = S.E;
    G = S.G;    I = S.I;
    a = S.a;    L = S.L;
    Area = S.Area;

    F = P/2;
    A = [P/(12*E*I) 0 P*a*(a-L)/(4*E*I)-theta 0];
    B = [0  P*a/(4*E*I) -P*a*L/(4*E*I) P*a^3/(12*E*I)-theta*a];
    C = [-P/(12*E*I) P*L/(4*E*I) -P*(L^2-a*L+a^2)/(4*E*I)+theta ...
        P*L*(L^2-3*a*L+3*a^2)/(12*E*I)-theta*L];

    x_size  = size(x);
```

```
    vb      = zeros(x_size(1),1);
    vs      = zeros(x_size(1),1);
    v       = zeros(x_size(1),1);
    for ix = 1:x_size(1)
        xp = x(ix);
        if xp<=a
            vb(ix)  = polyval(A,xp);
            vs(ix)  = -2*F*xp/(Area*G);
            v(ix)   = vb(ix)+vs(ix);
        elseif xp <= (L-a)
            vb(ix)  = polyval(B,xp);
            vs(ix)  = -2*F*a/(Area*G);
            v(ix)   = vb(ix)+vs(ix);
        else
            vb(ix)  = polyval(C,xp);
            vs(ix)  = -2*F*(L-xp)/(Area*G);
            v(ix)   = vb(ix)+vs(ix);
        end
    end
end
```

BIBLIOGRAPHY

Aboshio, A., Green, S., and Ye, J., "Experimental investigation of the mechanical properties of neoprene coated nylon woven reinforced composites," *Composite Structures*, vol. 120, pp. 386–393, 2015.

Barnfield, L., "Inflatable hangars and structures," Lindstrand Technologies, 2016, accessed on 4-05-2019. [Online]. Available: https://www.lindstrandtech.com/what-we-do/inflatable-structures/air-cell-structures/inflatable-hangars-shelters/

Blaber, J., Adair, B., and Antoniou, A., "Ncorr: Open-source 2d digital image correlation matlab software," *Experimental Mechanics*, 2015.

Budynas, R. G. and Nisbett, J. K., *Shigley's Mechanical Engineering Design*, 9th ed. New York, NY: McGraw-Hill, 2011, ch. 4, pp. 87–92,162–169.

Cavallaro, P. V., Hart, C. J., and Sadegh, A. M., "Mechanics of air-inflated drop-stitch fabric panels subject to bending loads," in *ASME International Mechanical Engineering Congress and Exposition*, San Diego, CA, 11 2013.

Cavallaro, P. V., Sadegh, A. M., and Quigley, C. J., "Decrimping behavior of uncoated plain-woven fabrics subjected to combined biaxial tension and shear stresses," *Textile Research Journal*, vol. 77(6), pp. 403–416, June 2007.

Collins, J., Rusby, H. R., and Staab, G. H., *Mechanical Design of Machine Elements and Machines: A Failure Prevention Perspective*, 2nd ed. Hoboken, NJ: Wiley, 2010, ch. 4, pp. 123–137.

Comer, R. and Levy, S., "Deflections of an inflated circular cylindrical cantilever beam," *American Institute of Aeronautics and Astronautics (AIAA) Journal*, vol. 1(7), pp. 1652–1655, 1963.

DiGiovanna, L., "Characterizing the mechanical properties of drop stitch inflatable structures," Massachusetts Institute of Technology, 2013, bachelor's thesis.

Falls, J. and Waters, J., "Bending tests of inflatable dropstitch panels," in *11th International Conference on Fast Sea Transportation, FAST*, 2011.

Felicissimo, R., "Exploration of the mechanical properties of both ridged and inflated drop stitch fabric material," Master's thesis, City University of New York, 2015.

Ferrazzoli, M., Navatek, 2018-2019, data set, personal correspondence.

Graczykowski, C. and Heinonen, J., "Adaptive inflatable structures for protecting wind turbines against ship collisions," IPPT - Institute of Fundamental Technology Research (Poland), Tech. Rep. VVT Working Papers 59, September 2006.

Halswell, P., Wilson, P., and Taunton, D., "Hydroelastic inflatable boats: Relevant literature and new design considerations," *International Journal of Small Craft Technology*, vol. 154 (B1), 2012.

Harilal, R. and Ramji, M., "Adaptation of open source 2d dic software ncorr for solid mechanics applications," Indian Institute of Technology, Tech. Rep., November 2014.

Ho, Q. D., "An assessment of the accuracy of the euler-bernoulli beam theory for calculating strain and deflection in composite sandwich beams," Master's thesis, University of New Orleans, 2015.

Hodge, J., "Sea eagle 472rl razorlite inflatable drop stitch kayak," Sea Eagle, 2018, accessed on 4-05-2019. [Online]. Available: https://www.seaeagle.com/RazorLite/473rl

Hulton, A. W., Cavallaro, P. V., and Hart, C. J., "Modal analyis and experimental testing of air-inflated dropstitch fabric structures used in marine applications," in *Proceedings of 2017 International Mechanical Engineering Congress and Exposition*, November 2017.

Hursa, A., Rolich, T., and Ražić, S. E., "Determining pseudo poisson's ratio of woven fabric with a digital image correlation method," *Textile Research Journal*, vol. 79, no. 17, pp. 1588–1598, 2009. [Online]. Available: https://doi.org/10.1177/0040517509104316

Justusson, B. P., Spagnuolo, D. M., and Yu, J. H., "Assessing the applicability of digital image correlation (dic) technique in tensile testing of fabric composites," Army Research Laboratory, Tech. Rep., February 2013.

Kelly, P., "Engineering solid mechanics," University of Auckland, 2015, accessed on 3-21-2019. [Online]. Available: http://homepages.engineering.auckland.ac.nz/~pkel015/SolidMechanicsBooks/

Li, Y. and Barbič, J., "Stable orthotropic materials," in *Proceedings of the ACM SIGGRAPH/Eurographics Symposium on Computer Animation*, ser. SCA '14. Aire-la-Ville, Switzerland, Switzerland: Eurographics Association, 2014, pp. 41–46. [Online]. Available: http://dl.acm.org/citation.cfm?id=2849517.2849524

Main, J., Peterson, S., and Strauss, A., "Load-deflection behavior of space-based inflatable fabric beams," *Journal of Aerospace Engineering*, vol. 7(2), pp. 225–238, April 1994.

Majumdar, A., "Fabric manufacturing - i," Indian Institute of Technology Dehli, August 2014, accessed on 4-05-2019. [Online]. Available: https://nptel.ac.in/courses/116102005/1

Roylance, D., "Mechanical properties of materials," Massachusetts Institute of Technology, 2008, accessed on 3-21-2019. [Online]. Available: http://web.mit.edu/course/3/3.225/book.pdf

Roylance, D., "Laminate composite plates," Massachusetts Institute of Technology, February 2010, accessed on 3-21-2019. [Online]. Available: https://ocw.mit.edu/courses/materials-science-and-engineering/3-11-mechanics-of-materials-fall-1999/modules/MIT3_11F99_laminates.pdf

Sadegh, A. M. and Cavallaro, P. V., "Air-inflated fabric structures," in *Mark's Standard Handbook for Mechanical Engineers*, 11st ed. McGraw-Hill, 2006, pp. 20.108–20.118.

Sadegh, A. M. and Cavallaro, P. V., "Mechanics of energy absorbability in plain-woven fabrics," *Journal of Engineered Fibers and Fabrics*, vol. 62, pp. 495–509, March 2012.

Taggart, D. G., "Simulation models for drop stitch inflatable panels," April 2018, unpublished, presentation.

Van, A. L. and Wielgosz, C., "Bending and buckling of inflatable beams: Some theoretical results," *Thin-Walled Structures*, vol. 43(8), pp. 1166–1187, 2005.